Fast convolution with the free space Helmholtz Green's function ☆

Gregory Beylkin *, Christopher Kurcz, Lucas Monzón

Department of Applied Mathematics, University of Colorado at Boulder, 526 UCB, Boulder, CO 80309-0526, United States

ARTICLE INFO

ABSTRACT

We construct an approximation of the free space Green's function for the Helmholtz equation that splits the application of this operator between the spatial and the Fourier domains, as in Ewald's method for evaluating lattice sums. In the spatial domain we convolve with a sum of decaying Gaussians with positive coefficients and, in the Fourier domain, we multiply by a band-limited kernel. As a part of our approach, we develop new quadratures appropriate for the singularity of Green's function in the Fourier domain. The approximation and quadratures yield a fast algorithm for computing volumetric convolutions with Green's function in dimensions two and three. The algorithmic complexity scales as $\mathcal{O}(\kappa^d \log \kappa + C(\log \epsilon^{-1})^d)$, where ϵ is selected accuracy, κ is the number of wavelengths in the problem, d is the dimension, and C is a constant. The algorithm maintains its efficiency when applied to functions with singularities. In contrast to the Fast Multipole Method, as $\kappa \rightarrow 0$, our approximation makes a transition to that of the free space Green's function for the Poisson equation. We illustrate our approach with examples.

© 2008 Elsevier Inc. All rights reserved.

1. Introduction

In many applied fields including acoustics, quantum mechanics, and electromagnetics, we encounter the need to compute convolutions with the free space Helmholtz Green's function. In these fields problems of interest often involve media or potentials described by functions with discontinuities or singularities. However, it is difficult to construct fast and accurate algorithms to compute convolutions with such functions entirely in spatial or entirely in the Fourier domain. In the spatial domain, a straightforward discretization of Green's function results in dense matrices, whereas in the Fourier domain slow decay of the product requires an unreasonably large computational domain to obtain accurate results. For these reasons, our

approach to obtain a fast and accurate algorithm is based on approximating Green's function so that its application is split between the spatial and Fourier domains.

We consider the problem of convolving a given function f with the free space Helmholtz Green's function G,

$$u(\mathbf{x}) = \int_{\mathbb{R}^d} G(\mathbf{x} - \mathbf{y})f(\mathbf{y})d\mathbf{y}, \tag{1}$$

where G satisfies

$$(\Delta + \kappa^2)G(\mathbf{x}) = -\delta(\mathbf{x}) \tag{2}$$

and the Sommerfeld condition

$$\lim_{|\mathbf{x}| \to \infty} |\mathbf{x}|^{\frac{d-1}{2}}\left(\frac{\partial G}{\partial |\mathbf{x}|} - i\kappa G\right) = 0, \quad \kappa > 0. \tag{3}$$

We assume that $f \in L^p(D)$ for some $1 \leqslant p \leqslant \infty$, and is supported in a bounded domain D. The function u is the solution to

$$(\Delta + \kappa^2)u(\mathbf{x}) = -f(\mathbf{x}) \tag{4}$$

and satisfies the Sommerfeld condition.

In dimension d, the free space Helmholtz Green's function is given by

$$G(\mathbf{x}) = \frac{i}{4}\left(\frac{\kappa}{2\pi|\mathbf{x}|}\right)^{(d-2)/2} H_{(d-2)/2}^{(1)}(\kappa|\mathbf{x}|),$$

where $H_{(d-2)/2}^{(1)}$ is a Hankel function of the first kind and $|\mathbf{x}| = \left(\sum_{j=1}^d x_j^2\right)^{1/2}$ denotes the Euclidean norm of the vector $\mathbf{x}$. We focus our attention on dimensions $d = 3$ and $d = 2$, so that

$$G(\mathbf{x}) = \begin{cases} \frac{1}{4\pi}\frac{e^{i\kappa|\mathbf{x}|}}{|\mathbf{x}|} & \text{for dimension } d = 3, \\ \frac{i}{4}H_0^{(1)}(\kappa|\mathbf{x}|) & \text{for dimension } d = 2. \end{cases} \tag{5}$$

Our algorithm is designed to maintain its performance when applied to compactly supported functions with singularities and/or discontinuities. For volumetric convolutions the algorithmic complexity scales as $\mathcal{O}(\kappa^d \log \kappa + C(\log \epsilon^{-1})^d)$, where ϵ is the user-selected accuracy and C is a constant.

In our approach we separate the real and imaginary parts of Green's function and approximate them in different ways. The real part is approximated as a sum of two terms which are applied separately, one in the spatial and the other in the Fourier domain. We note that this splitting between domains is the key idea in Ewald's method for evaluating lattice sums [1], and we elaborate further on this connection later (see also [2]).

The resulting approximation in the spatial domain is a sum of decaying Gaussians with positive coefficients. It is a natural extension of a separated representation for the free space Poisson Green's function, i.e., $\kappa = 0$ in (5), as a sum of Gaussians [3,4]. For the Poisson Green's function such approximation leads to fast algorithms for its application [5–7]. In the spatial domain, we may use these algorithms as well as the fast Gauss transform in [8–10].

The approximation in the Fourier domain decays exponentially fast and is effectively band-limited. Since the kernel and its approximation are radially symmetric, we construct quadratures in a ball incorporating the kernel as a part of the measure (see also [11]). The resulting trigonometric sums are then evaluated using the Unequally Spaced Fast Fourier Transform (USFFT) [12–14], yielding a fast algorithm. The imaginary part of Green's function is a delta function on the sphere of radius κ. With integration limited to a sphere, we also use the USFFT to compute the trigonometric sum resulting from our discretization.

Our approach yields a fast algorithm for computing volumetric integrals and has the same complexity as the Fast Multipole Method (FMM) [15–17] for such problems. Although the FMM was originally designed to solve boundary integral equations, it may also be used to compute volumetric integrals. We note that FMM relies on a directional approximation and the diagonalization of translations whereas our approximation of Green's function is radially symmetric. Also, as it stands, FMM approximation differs for problems with large or small κ. Indeed, the high frequency approximation used in the FMM [15] breaks down as $\kappa \to 0$ and is replaced by an alternative in [16,17] for the low frequency regime. We note that our approach, as $\kappa \to 0$, transitions to the Poisson problem without difficulty.

Beyond the FMM, there is a vast literature regarding algorithms for applying Green's function. Let us mention several approaches for computing volumetric convolutions with Green's function, typically described in the context of computing solutions to the Lippmann–Schwinger equation. If the convolution is computed with a smooth rapidly decaying or periodic function, then it is natural to compute the result entirely in the Fourier domain, an approach sometimes referred to as CGFFT (see e.g. [18]). Applying this approach to functions with singularities presents difficulties either with maintaining accuracy or with the cost of computation due to the slow decay of both the function and the kernel in the Fourier domain. There have been a number of proposals to address these issues by using high order discretizations. In [19] the authors transform the equation to polar coordinates and use the addition theorem for Hankel functions to separate the radial and angular integration. The procedure artificially band-limits Green's function asserting that, for discontinuous scattering potentials, the error

is inversely proportional to the square of the band-limit (see [19, Corollary 3.9]). The method in [20] also constructs a band-limited version of Green's function and suffers from similar accuracy problems for discontinuous scattering potentials (see [20, Theorem 2]). The approach in [21] is based on an approximation of sufficiently smooth functions by a collection of equally spaced Gaussians of fixed width. Given such an approximation, convolutions of Gaussians with Green's function are computed analytically. However, the effectiveness of this representation (or, alternatively, the accuracy of the result) depends on the smoothness of the function (see [21, Theorems 1 and 2]), which renders the method ineffective for discontinuous functions. We note that in the context of solving the Lippmann–Schwinger equation, direct methods [22] have also been developed. The algorithmic complexity for determining the scattered field as a solution of the Lippmann–Schwinger equation is $\mathcal{O}(\kappa^3)$ in dimension $d = 2$.

We would like to emphasize two distinctive features of our approach. First, we guarantee user-selected finite accuracy ϵ. Since the cost of computation depends only weakly on accuracy, as $(\log \epsilon^{-1})^d$, the algorithm remains efficient even when applying the operator to functions with discontinuities. This should be compared with methods where the cost is estimated in terms of their order p, yielding a cost proportional to $(\epsilon^{-1})^{d/p}$. Second, we note that algorithms for the quasi-periodic Green's function and those incorporating boundary conditions on simple domains have the same structure and complexity as those of this paper and have been developed in [2].

The paper is organized as follows. In Section 2, we provide appropriate definitions and introduce our notation. In Section 3, we formulate and state the main results as two theorems. Then, in Section 4, we outline proofs of these theorems by organizing them as a sequence of propositions with technical details deferred to the Appendix. Next, in Section 5, we construct quadratures in the Fourier domain for the efficient application of radially symmetric kernels. We describe a fast algorithm for applying Green's function and illustrate our approach with examples in Section 6. Finally, we summarize our results in Section 7 and collect proofs in the Appendix.

2. Preliminaries

2.1. Fourier transform of radial functions

We define the Fourier transform in dimension d as

$$\hat{f}(\mathbf{p}) = \int_{\mathbb{R}^d} f(\mathbf{x}) e^{-i\mathbf{x}\cdot\mathbf{p}} \, d\mathbf{x} \tag{6}$$

and its inverse as

$$f(\mathbf{x}) = \frac{1}{(2\pi)^d} \int_{\mathbb{R}^d} \hat{f}(\mathbf{p}) e^{i\mathbf{x}\cdot\mathbf{p}} \, d\mathbf{p}. \tag{7}$$

For a radially symmetric function f, we use the same notation for the multi-dimensional and the associated one-dimensional function, $f(\mathbf{x}) = f(|\mathbf{x}|)$ and note that $\hat{f}(\mathbf{p})$ is also a radially symmetric function satisfying

$$f(r) = \frac{1}{(2\pi)^{d/2} r^{d/2-1}} \int_0^\infty \hat{f}(\rho) \rho^{d/2} J_{d/2-1}(\rho r) d\rho, \tag{8}$$

where $r = |\mathbf{x}|$ and $\rho = |\mathbf{p}|$. For convenience, we explicitly write (8) for dimension $d = 3$

$$f(r) = \frac{1}{2\pi^2 r} \int_0^\infty \hat{f}(\rho) \sin(\rho r) \rho \, d\rho \tag{9}$$

and dimension $d = 2$

$$f(r) = \frac{1}{2\pi} \int_0^\infty \hat{f}(\rho) J_0(\rho r) \rho \, d\rho. \tag{10}$$

2.2. Free space Green's function for the Helmholtz equation

On taking the Fourier transform of Green's function (2), we obtain

$$\widehat{G}(\mathbf{p}) = \frac{1}{|\mathbf{p}|^2 - \kappa^2}, \tag{11}$$

where $\mathbf{p} \in \mathbb{R}^d$. The inverse Fourier transform of $\widehat{G}$ is a singular integral and its usual regularization

$$G^\pm(\mathbf{x}) = \lim_{\lambda \to 0^+} \frac{1}{(2\pi)^d} \int_{\mathbb{R}^d} \frac{e^{i\mathbf{x}\cdot\mathbf{p}}}{|\mathbf{p}|^2 - \kappa^2 \mp i\lambda} \, d\mathbf{p} \tag{12}$$

yields the outgoing and incoming Green's functions

$$G^{\pm}(\mathbf{x}) = \frac{1}{4\pi} \frac{e^{\pm i\kappa|\mathbf{x}|}}{|\mathbf{x}|} \tag{13}$$

in dimension $d = 3$ and

$$G^{\pm}(\mathbf{x}) = \frac{i}{4} H_0^{(1)}(\pm\kappa|\mathbf{x}|) = -\frac{1}{4} Y_0(\pm\kappa|\mathbf{x}|) + \frac{i}{4} J_0(\pm\kappa|\mathbf{x}|) \tag{14}$$

in dimension $d = 2$.

Instead of (12), we prefer to use a different regularization which yields the same result, namely

$$G^{\pm}(\mathbf{x}) = \lim_{\lambda \to 0^+} \frac{1}{(2\pi)^d} \int_{\mathbb{R}^d} \frac{e^{i\mathbf{x}\cdot\mathbf{p}}}{|\mathbf{p}|^2 - (\kappa \pm i\lambda)^2} d\mathbf{p}. \tag{15}$$

For a proof see Appendix A.1.

We note that the outgoing Green's function G^+ in (13) and (14) satisfies the Sommerfeld radiation condition (3). In what follows we consider only the outgoing Green's function (5) and drop the $\pm$ notation. Let us define

$$\widehat{G}(\rho, \lambda) = \frac{1}{\rho^2 - (\kappa + i\lambda)^2} \tag{16}$$

and write its real and imaginary parts as

$$\mathcal{R}_e(\widehat{G}(\rho, \lambda)) = \frac{1}{2\rho} \left(\frac{\rho - \kappa}{(\rho - \kappa)^2 + \lambda^2} + \frac{\rho + \kappa}{(\rho + \kappa)^2 + \lambda^2} \right) \tag{17}$$

and

$$\mathcal{I}_m(\widehat{G}(\rho, \lambda)) = \frac{1}{2\rho} \left(\frac{\lambda}{(\rho - \kappa)^2 + \lambda^2} - \frac{\lambda}{(\rho + \kappa)^2 + \lambda^2} \right). \tag{18}$$

We observe that in the limit

$$\lim_{\lambda \to 0^+} \mathcal{I}_m(\widehat{G}(\rho, \lambda)) = \frac{\pi}{2\rho} (\delta(\rho - \kappa) - \delta(\rho + \kappa)) \tag{19}$$

is a generalized function (see e.g. [23, Chapter III, Section 1.3]) which corresponds to integration over the d-dimensional sphere. As $\kappa \to 0$, the imaginary part vanishes and we attain the fundamental solution for the Poisson equation.

Note that (see e.g. [24, Section 4.1])

$$\lim_{\lambda \to 0^+} \int_0^\infty \frac{1}{2\rho} \left(\frac{\rho - \kappa}{(\rho - \kappa)^2 + \lambda^2} + \frac{\rho + \kappa}{(\rho + \kappa)^2 + \lambda^2} \right) d\rho = \text{p.v.} \int_0^\infty \frac{1}{\rho^2 - \kappa^2} d\rho, \tag{20}$$

where the principal value is considered about $\rho = \kappa$, so that

$$\mathcal{R}_e(G(\mathbf{x})) = \frac{1}{(2\pi)^d} \text{p.v.} \int_{\mathbb{R}^d} \frac{e^{i\mathbf{x}\cdot\mathbf{p}}}{|\mathbf{p}|^2 - \kappa^2} d\mathbf{p} = \frac{1}{(2\pi)^d} \lim_{\lambda \to 0^+} \int_{\mathbb{R}^d} \mathcal{R}_e(\widehat{G}(|\mathbf{p}|, \lambda)) e^{i\mathbf{x}\cdot\mathbf{p}} d\mathbf{p} \tag{21}$$

and

$$\mathcal{I}_m(G(\mathbf{x})) = \frac{\pi}{2(2\pi)^d} \int_{\mathbb{R}^d} \frac{\delta(|\mathbf{p}| - \kappa)}{|\mathbf{p}|} e^{i\mathbf{x}\cdot\mathbf{p}} d\mathbf{p} = \frac{1}{(2\pi)^d} \lim_{\lambda \to 0^+} \int_{\mathbb{R}^d} \mathcal{I}_m(\widehat{G}(|\mathbf{p}|, \lambda)) e^{i\mathbf{x}\cdot\mathbf{p}} d\mathbf{p}. \tag{22}$$

3. Approximation of the real part of Green's function

Our goal is to approximate the real part of Green's function (21) in order to compute convolutions

$$(\mathcal{R}_e(G) * f)(\mathbf{x}) = \frac{1}{(2\pi)^d} \text{p.v.} \int_{\mathbb{R}^d} \widehat{G}(\mathbf{p}) \hat{f}(\mathbf{p}) e^{i\mathbf{x}\cdot\mathbf{p}} d\mathbf{p}$$

in a fast and accurate manner. We split this operator into two, one acting as a well localized convolution in the spatial domain and the other as multiplication by an (effectively) compactly supported function in the Fourier domain. We write

$$\widehat{G}(\rho) = \widehat{F}_{\text{sing}}(\rho) + \widehat{F}_{\text{oscill}}(\rho), \tag{23}$$

where

$$\widehat{F}_{\text{sing}}(\rho) = \frac{1 - e^{-\alpha^2(\rho^2 - \kappa^2)/\kappa^2}}{\rho^2 - \kappa^2},$$

$$\widehat{F}_{\text{oscill}}(\rho) = \frac{e^{-\alpha^2(\rho^2 - \kappa^2)/\kappa^2}}{\rho^2 - \kappa^2}$$

(24)

and α is a real parameter to be selected later. Next, we outline the approximation and application of $\widehat{F}_{\text{sing}}$ and $\widehat{F}_{\text{oscill}}$ with the details of estimates and associated parameter choices deferred to following sections.

Using

$$\frac{1 - e^{-\alpha^2(\rho^2 - \kappa^2)/\kappa^2}}{\rho^2 - \kappa^2} = 2 \int_{-\infty}^{\log\frac{\alpha}{\kappa}} e^{-(\rho^2 - \kappa^2)e^{2s} + 2s} \, ds,$$

we transform $\widehat{F}_{\text{sing}}$ to the spatial domain to obtain

$$F_{\text{sing}}(r) = \frac{1}{2^{d-1}\pi^{d/2}} \int_{-\log\frac{\alpha}{\kappa}}^{\infty} e^{-r^2\frac{e^{2s}}{4} + \kappa^2 e^{-2s} + (d-2)s} \, ds.$$

(25)

We then approximate F_{sing} in the region $r \geq \delta_0 > 0$ by a sum of decaying Gaussians with positive coefficients,

$$S_{\text{sing}}(r) = \sum_{n=1}^{N} q_n e^{-\sigma_n r^2}.$$

(26)

Thus, convolutions with F_{sing} are approximated by

$$(S_{\text{sing}} * f)(\mathbf{x}) = \sum_{n=1}^{N} q_n \int_D e^{-\sigma_n |\mathbf{x} - \mathbf{y}|^2} f(\mathbf{y}) d\mathbf{y}.$$

Turning to $\widehat{F}_{\text{oscill}}$, we define

$$\widehat{S}_{\text{oscill}}(\rho) = \begin{cases} \frac{e^{-\alpha^2(\rho^2 - \kappa^2)/\kappa^2}}{2\rho} \sum_{m=1}^{M} w_m \left((\rho - \kappa)e^{-\tau_m(\rho - \kappa)^2} + (\rho + \kappa)e^{-\tau_m(\rho + \kappa)^2} \right), & 0 \leq \rho \leq b\kappa, \\ 0, & b\kappa < \rho, \end{cases}$$

(27)

which, as we show below, accurately approximates $\widehat{F}_{\text{oscill}}$ in the region $|\rho - \kappa| \geq \min\{\kappa\delta, \delta\}$, where $b > 1$ and $\delta > 0$ are parameters chosen later. The inverse Fourier transform of $\widehat{S}_{\text{oscill}}$ is given by

$$S_{\text{oscill}}(r) = \frac{1}{(2\pi)^{d/2} r^{d/2-1}} \int_0^{b\kappa} \widehat{S}_{\text{oscill}}(\rho) \rho^{d/2} J_{d/2-1}(\rho r) d\rho$$

(28)

and we use it as an approximation to

$$F_{\text{oscill}}(r) = \frac{1}{(2\pi)^{d/2} r^{d/2-1}} \text{p.v.} \int_0^{\infty} \widehat{F}_{\text{oscill}}(\rho) \rho^{d/2} J_{d/2-1}(\rho r) d\rho.$$

(29)

Thus, convolutions with F_{oscill} are approximated in the Fourier domain as

$$(S_{\text{oscill}} * f)(\mathbf{x}) = \frac{1}{(2\pi)^d} \int_{|\mathbf{p}| \leq b\kappa} \widehat{S}_{\text{oscill}}(|\mathbf{p}|) \hat{f}(\mathbf{p}) e^{i\mathbf{x} \cdot \mathbf{p}} d\mathbf{p}.$$

As a result, we approximate the real part of Green's function as

$$\widetilde{G}_R(r) = S_{\text{sing}}(r) + S_{\text{oscill}}(r).$$

(30)

The function S_{sing} captures the singularity of the real part of Green's functions (13) and (14) at $r = 0$ and S_{oscill} their oscillations.

Let us now state the main results of the paper.

Theorem 1. *For any $\epsilon > 0$ we may select parameters $\delta, \delta_0, M, b, \alpha = \alpha(b, \delta)$, and N in (23)–(30), so that for $r \geq \delta_0 > 0$ we have*

$$|\mathcal{R}e(G(r)) - \widetilde{G}_R(r)| \leq \epsilon \left(1 + \frac{1}{r} \right)$$

(31)

in dimension $d = 3$, and

$$|\mathcal{R}e(G(r)) - \widetilde{G}_R(r)| \leq \epsilon \left(1 + \log \left(1 + \frac{1}{r^2} \right) + \sqrt{r} \right)$$

(32)

in dimension $d = 2$.

The proof is given in Section 4. Using Theorem 1, the convolution with the real part of Green's function in a bounded domain is estimated via

Theorem 2. *Let $D \subset \mathbb{R}^d, d = 2, 3$, be a bounded domain such that $\text{diam}(D) \leq 1$. Given $\epsilon > 0$, $\widetilde{G}_R$ as in Theorem 1 and $f \in L^p(D)$ for $1 \leq p \leq \infty$, we have*

$$\|(\mathcal{R}_\epsilon(G) - \widetilde{G}_R) * f\|_{L^p(D)} \leqslant \epsilon \|f\|_{L^p(D)}.$$

The proof is given in Section 4 and follows from Theorem 1.

Our approximation leads to fast methods for convolutions with the real part of Green's functions (13) or (14) which we discuss in detail in Section 6. Briefly, since S_{sing} is a sum of Gaussians, there are several fast algorithms available for its application, e.g. [7] or the fast Gauss transform [8–10]. The second term, S_{oscill} in (30), is applied in the Fourier domain as a multiplication operator. For this purpose, following [25,11], we construct quadratures incorporating $\widehat{S}_{\text{oscill}}$ as part of the measure to compute the integral and evaluate the resulting trigonometric sums using the USFFT (see [12–14]). Since $\widehat{S}_{\text{oscill}}$ decays rapidly, we do not require decay of the Fourier transform of the function to which we apply Green's function. Thus, we do not need to impose any smoothness requirements on the function to maintain accuracy.

Remark 3. The imaginary part of Green's function is not singular and, thus, does not require any special representation. Applying this operator in the Fourier domain reduces to an integral on a sphere of radius κ, which is discretized using an appropriate quadrature for the sphere (e.g. the trapezoidal rule in dimension $d = 2$, see Section 6 for details).

Remark 4. A naive attempt to separate the singularity in (13) by considering e.g. $(\cos(\kappa r) - 1)/r + 1/r$, does not yield the same effect. Observe that $(\cos(\kappa r) - 1)/r$ has a discontinuous first derivative at zero when extended evenly and, therefore, its Fourier transform does not decay sufficiently fast. Alternative splittings appear in the so-call particle mesh Ewald (when $\kappa = 0$, see e.g. [26]) and use the complementary error function in space; other possible splittings are described in e.g. [27]. We find that these splittings do not lead to an analytic form conducive for our purposes.

3.1. Alternative derivation using Ewald's approach

Another approach for arriving at (25) and (29) is by mimicking Ewald's method [1]. For brevity, we consider only dimension $d = 3$. Ewald's approach uses the integral

$$\frac{1}{4\pi} \frac{e^{i\kappa r}}{r} = \frac{1}{2\pi^{3/2}} \int_\Gamma e^{-r^2 t^2 + \frac{\kappa^2}{4t^2}} \, dt, \tag{33}$$

where Γ is an appropriately chosen contour. Instead of (33) (and similar to Green's function derivation in Section 2.2), we add an imaginary part to κ, $\kappa + i\lambda$ with $\lambda > \kappa$, and consider

$$\frac{1}{4\pi} \frac{e^{i(\kappa+i\lambda)r}}{r} = \frac{1}{2\pi^{3/2}} \int_0^\infty e^{-r^2 t^2 + \frac{(\kappa+i\lambda)^2}{4t^2}} \, dt. \tag{34}$$

The expression on the left side of the formula yields Green's function as $\lambda \to 0^+$, whereas the integral on the right side is well defined only for $\lambda > \kappa$. To obtain (34) we use the primitive

$$\frac{1}{2\pi^{3/2}} \int e^{-r^2 t^2 + \frac{(\kappa+i\lambda)^2}{4t^2}} dt = -\frac{e^{(-i\kappa+\lambda)r}}{8\pi r} \operatorname{erfc}\left(\frac{-i\kappa+\lambda}{2t} + rt\right) + \frac{e^{(i\kappa-\lambda)r}}{8\pi r} \operatorname{erfc}\left(\frac{-i\kappa+\lambda}{2t} - rt\right)$$

and [28, 7.1.16] to evaluate

$$\lim_{t \to 0^+} -\frac{e^{(-i\kappa+\lambda)r}}{8\pi r} \operatorname{erfc}\left(\frac{-i\kappa+\lambda}{2t} + rt\right) + \frac{e^{(i\kappa-\lambda)r}}{8\pi r} \operatorname{erfc}\left(\frac{-i\kappa+\lambda}{2t} - rt\right) = 0$$

and

$$\lim_{t \to \infty} -\frac{e^{(-i\kappa+\lambda)r}}{8\pi r} \operatorname{erfc}\left(\frac{-i\kappa+\lambda}{2t} + rt\right) + \frac{e^{(i\kappa-\lambda)r}}{8\pi r} \operatorname{erfc}\left(\frac{-i\kappa+\lambda}{2t} - rt\right) = \frac{1}{4\pi} \frac{e^{(i\kappa-\lambda)r}}{r}.$$

As in Ewald's method, let us introduce a real parameter $\eta > 0$ to split the region of integration in (34) into two intervals $(0, \eta)$ and (η, ∞). In the interval $(0, \eta)$, the Fourier transform (9) yields

$$\frac{1}{2\pi^{3/2}} \int_0^\eta e^{-r^2 t^2 + \frac{(\kappa+i\lambda)^2}{4t^2}} dt = \frac{1}{4\pi^2 r} \int_0^\eta \int_0^\infty e^{\frac{-\rho^2 + (\kappa+i\lambda)^2}{4t^2}} \sin(\rho r) \rho \, d\rho \frac{dt}{t^3}.$$

Since $\lambda > \kappa$, we are free to switch the order of integration to obtain

$$\frac{1}{4\pi^2 r} \int_0^\infty \int_0^\eta e^{\frac{-\rho^2 + (\kappa+i\lambda)^2}{4t^2}} \frac{dt}{t^3} \sin(\rho r) \rho \, d\rho = \frac{1}{2\pi^2 r} \int_0^\infty \frac{e^{\frac{-\rho^2 + (\kappa+i\lambda)^2}{4\eta^2}}}{\rho^2 - (\kappa+i\lambda)^2} \sin(\rho r) \rho \, d\rho.$$

The resulting expression is well defined for any $\lambda > 0$ and, due to analytic dependence on λ, taking the limit $\lambda \to 0^+$ and using (20) and (19), we obtain

$$\frac{1}{2\pi^{3/2}}\lim_{\lambda\to 0^+}\int_0^\eta e^{-r^2 t^2+\frac{(\kappa+i\lambda)^2}{4t^2}}dt=\frac{1}{2\pi^2 r}\,\text{p.v.}\int_0^\infty \frac{e^{\frac{-\rho^2+\kappa^2}{4\eta^2}}}{\rho^2-\kappa^2}\sin(\rho r)\rho\,d\rho+i\frac{\sin(\kappa r)}{4\pi r}.$$

Setting $\eta=\kappa/(2\alpha)$, we recover (29) and the imaginary part of Green's function and, since the integral on the interval (η,∞) is well defined for $\lambda=0$, we recover (25) after the change of variable $t=e^s/2$.

We note that in dimension $d=2$ we may follow the same steps but starting (for $\lambda>\kappa$) with

$$\frac{i}{4}H_0^{(1)}((\kappa-i\lambda)r)=\frac{1}{2\pi}\int_0^\infty e^{-r^2 t^2+\frac{(\kappa+i\lambda)^2}{4t^2}}\frac{dt}{t}$$

instead of (34).

4. Estimates for Theorems 1 and 2

In this section, we provide the estimates required to obtain Theorems 1 and 2. The proof is split into a sequence of propositions:

(1) Proposition 5 provides estimates for the error due to removing a small interval around the singularity at $\rho=\kappa$ in (29) and limiting the integration to a finite region, thus exploiting the exponential decay of $\widehat{F}_{\text{oscill}}$ in (24).
(2) Proposition 8 gives an estimate of the error due to the discretization of the integral defining F_{sing} in (25).
(3) Proposition 10 provides an estimate of the error of the approximation of $\widehat{F}_{\text{oscill}}$ in (24) by $\widehat{S}_{\text{oscill}}$ in (27).
(4) Proposition 11 provides an estimate of the error of the approximation in the spatial domain of F_{oscill} in (29) by S_{oscill} in (28).

The combination of these propositions yields a proof of Theorems 1 and 2. These estimates also allow us to select parameters b and α and elucidate their meaning.

In order to estimate the contribution of $\widehat{F}_{\text{oscill}}(\rho)$ near $\rho=\kappa$, we introduce

$$I_-(r)=\frac{1}{(2\pi)^{d/2}r^{d/2-1}}\int_0^{\kappa-\min\{\kappa\delta,\delta\}}\widehat{F}_{\text{oscill}}(\rho)\rho^{d/2}J_{d/2-1}(\rho r)d\rho \tag{35}$$

and

$$I_{+,b}(r)=\frac{1}{(2\pi)^{d/2}r^{d/2-1}}\int_{\kappa+\min\{\kappa\delta,\delta\}}^{b\kappa}\widehat{F}_{\text{oscill}}(\rho)\rho^{d/2}J_{d/2-1}(\rho r)d\rho \tag{36}$$

for $b\kappa>\kappa+\min\{\kappa\delta,\delta\}$. We have

Proposition 5. *For* $0<\delta\leqslant 1/3$ *and* $b\geqslant\sqrt{2}$, *let us select* α *in the definition of* $\widehat{F}_{\text{oscill}}$ *as*

$$\alpha^2=\frac{\log\delta^{-1}}{b^2-1}. \tag{37}$$

Then, for F_{oscill} *given in (29) and any* $r\geqslant 0$, *we have*

$$|F_{\text{oscill}}(r)-I_-(r)-I_{+,b}(r)|\leqslant\delta\log\delta^{-1}\left(2+\frac{1}{r}\right)$$

in dimension $d=3$, *and*

$$|F_{\text{oscill}}(r)-I_-(r)-I_{+,b}(r)|\leqslant\delta\log\delta^{-1}(3+\sqrt{r})$$

in dimension $d=2$.

The proof may be found in Appendix A.2. Proposition 5 allows us to select the parameter α given δ and b. Recall that the parameter b effectively limits the region of integration in the Fourier domain while δ controls the distance to the singularity at $\rho=\kappa$ (in practice $\delta\ll 1$). With α in (37) we ensure that $e^{-\alpha^2(\rho^2-\kappa^2)/\kappa^2}\leqslant\delta$ for $\rho\geqslant b\kappa$, which explains the choice of the upper limit in the integral (36).

Remark 6. As $\kappa\to 0, \widehat{F}_{\text{oscill}}\to 0$ and F_{sing} approaches the free space Green's function for the Poisson equation. Thus, to apply the operator with $\kappa=0$, we convolve only with F_{sing}. This constitutes the smooth transition of our approximation to that for Green's function for the Poisson equation.

Remark 7. Although we only require $b>1$, in practice the choice of this parameter does depend on κ and δ. One has to keep in mind that while selecting b close to 1 reduces the size of the region of integration in (36), it is also important to control the size of $\widehat{F}_{\text{oscill}}$ near zero as it may become large. By setting $\rho=0$ in (24) and α as in (37), we obtain
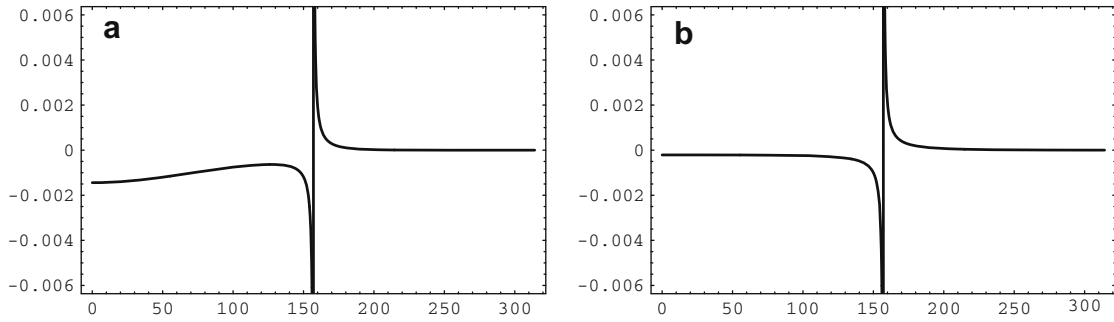
Fig. 1. Radially symmetric function $\widehat{F}_{\text{oscill}}$ (24) with $\kappa = 50\pi, \delta \approx 10^{-10}$ and (a) $b = 3$ or (b) $b = 5$.

$$\widehat{F}_{\text{oscill}}(0) = -\frac{1}{\kappa^2 \delta^{1/(b^2-1)}}.$$

Choosing the parameter b close to 1 may cause a loss of accuracy due to numerical cancellation as F_{sing} and F_{oscill} could be large and of opposite signs (see Fig. 4). Thus, by choosing b we strike a compromise between the size of the region of integration and the behavior of $\widehat{F}_{\text{oscill}}$ near zero. For moderate size κ we select $b \sim 3$; for large κ we may select a smaller b, and for small κ we do not need to compute in the Fourier domain at all (see previous remark). The impact of the choice of b is illustrated in Fig. 1.

Next, for the approximation of F_{sing} as a sum of Gaussians, we estimate the error of discretizing the integral in (25).

Proposition 8. *Given F_{sing} in (25), $0 < \epsilon \leqslant 1$ and $0 < \delta_0 \leqslant 1$, there exists a quadrature with positive parameters q_n and σ_n which define S_{sing} in (26) such that*

$$|F_{\text{sing}}(r) - S_{\text{sing}}(r)| \leqslant \begin{cases} \frac{1}{r} & \text{for } 0 \leqslant r < \delta_0, \\ \frac{\epsilon}{r} & \text{for } r \geqslant \delta_0 \end{cases} \tag{38}$$

in dimension $d = 3$ and

$$|F_{\text{sing}}(r) - S_{\text{sing}}(r)| \leqslant \begin{cases} \log\left(1 + \frac{1}{r^2}\right) & \text{for } 0 \leqslant r < \delta_0, \\ \epsilon \log\left(1 + \frac{1}{r^2}\right) & \text{for } r \geqslant \delta_0 \end{cases} \tag{39}$$

in dimension $d = 2$.

The proof may be found in Appendix A.3. As an example, we use the generalized Gaussian quadratures developed in [25, Section 7] associated with Prolate Spheroidal Wave Functions (PSWF). In Fig. 2, we plot the relative error estimated in Proposition 8 (for $d = 3$) using these quadratures. We note that the number of terms in (26) can be further reduced using the procedure in [3, Section 6].

Remark 9. In [3, Appendix A], $1/r$ is approximated by a sum of Gaussians using the trapezoid rule (as the first step) to discretize

$$\frac{1}{r} = \frac{2}{\sqrt{\pi}} \int_{-\infty}^{\infty} e^{-r^2 e^{2s} + s} \, ds.$$

This yields an accurate discretization for $r \in [\delta_0, 1]$ due to the decay of the integrand and its derivatives. We note that this integral and the one used to define F_{sing} in (25) differ only by the introduction of the parameter κ and a finite endpoint. Although this endpoint requires us to consider quadratures other than the trapezoid rule, we obtain a comparable number of nodes to that estimated and reported in [3,29] for approximating $1/r$. We display the number of terms, N in (25), as a function of ϵ and κ in Table 1.

In the next proposition we construct a smooth approximation of $\widehat{F}_{\text{oscill}}$ in (24).

Proposition 10. *Given $0 < \delta \leqslant 1$ and $b > 1$, consider $\widehat{F}_{\text{oscill}}$ with α chosen as in (37). For any $0 < \epsilon_0 \leqslant 1$ there exists $w_m > 0$ and $\tau_m > 0$ defining $\widehat{S}_{\text{oscill}}$ in (27) such that*

$$|\widehat{F}_{\text{oscill}}(\rho) - \widehat{S}_{\text{oscill}}(\rho)| \leqslant \epsilon_0 \frac{\kappa e^{-\alpha^2(\rho^2 - \kappa^2)/\kappa^2}}{\rho(\kappa^2 - \rho^2)} \tag{40}$$
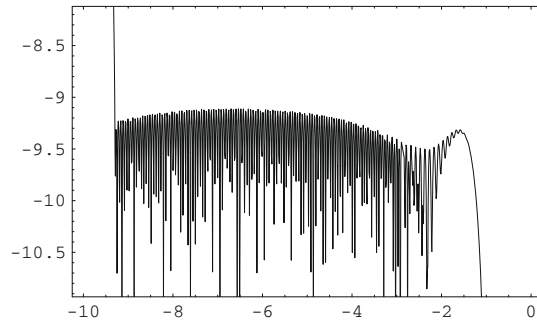
Fig. 2. Relative error in discretization of the spatial part of the approximation (25) for dimension $d = 3$ with parameters $\kappa = 50\pi, \epsilon \approx 10^{-9}, \delta_0 \approx 10^{-9}$ and $\alpha \approx 2$, using $\log_{10}$ scale on both axes.

Table 1
Number of Gaussians in the spatial part approximation (26) in dimension $d = 3$. We have chosen $b = 3, \alpha^2 = \frac{\log \epsilon^{-1}}{b^2 - 1}$, and $\delta_0 = \sqrt{\epsilon}$. We observe (and explain further in the text) that the number of Gaussians depends logarithmically on ϵ and decreases as κ increases.

	$\kappa = 25$	$\kappa = 50$	$\kappa = 75$	$\kappa = 100$	$\kappa = 125$	$\kappa = 150$
$\epsilon = 10^{-3}$	12	10	8	6	5	4
$\epsilon = 10^{-6}$	40	36	34	32	31	30
$\epsilon = 10^{-9}$	66	64	62	60	58	58
$\epsilon = 10^{-12}$	90	88	86	84	83	83

for $0 \leqslant \rho \leqslant \kappa - \min\{\kappa\delta, \delta\}$ and

$$|\widehat{F}_{\text{oscill}}(\rho) - \widehat{S}_{\text{oscill}}(\rho)| \leqslant \epsilon_0 \frac{e^{-\alpha^2(\rho^2 - \kappa^2)/\kappa^2}}{\rho^2 - \kappa^2} \tag{41}$$

for $\kappa + \min\{\kappa\delta, \delta\} \leqslant \rho \leqslant b\kappa$. Furthermore

$$\sum_{m=1}^{M} w_m(\rho + \kappa)e^{-\tau_m(\rho + \kappa)^2} \leqslant \frac{2}{\rho + \kappa} \tag{42}$$

for $0 \leqslant \rho \leqslant b\kappa$ and

$$\sum_{m=1}^{M} w_m(\rho - \kappa)^2 e^{-\tau_m(\rho - \kappa)^2} \leqslant 2 \tag{43}$$

for $\kappa - \min\{\kappa\delta, \delta\} \leqslant \rho \leqslant \kappa + \min\{\kappa\delta, \delta\}$.

The proof of this proposition may be found in Appendix A.4.

Next, we estimate the spatial domain error introduced by this approximation. We assume that the parameters b and δ satisfy $b \geqslant \sqrt{3}$ and $0 < \delta \leqslant 1/3$.

Proposition 11. *Given sufficiently small $\epsilon > 0$, we select $b \geqslant \sqrt{3}$ and determine $0 < \delta \leqslant 1/3$ such that $\epsilon = 5\delta \log(c\delta^{-1})$, where $c = \max\{\kappa, 1\}(b^2 - 1)/2$. With these parameters chosen, we set α as in (37), select $\epsilon_0 = \delta/e^{\alpha^2}$ and construct $\widehat{S}_{\text{oscill}}$ in Proposition 10 and S_{oscill} in (28).*

Then, for $r \geqslant 0$, the error of approximating F_{oscill} in (29) is estimated as

$$|F_{\text{oscill}}(r) - S_{\text{oscill}}(r)| \leqslant \epsilon\left(1 + \frac{1}{r}\right)$$

in dimension $d = 3$, and

$$|F_{\text{oscill}}(r) - S_{\text{oscill}}(r)| \leqslant \epsilon\left(1 + \sqrt{r}\right)$$

in dimension $d = 2$.

The proof of the proposition is provided in Appendix A.5. We conclude this section with the proofs of our main results.

Proof of Theorem 1. The proof is obtained by combining the estimates from Propositions 8 and 11.　□

Proof of Theorem 2. Using Minkowski's inequality for convolutions (see e.g. [24, p. 20]), we have

$$\|(\mathcal{R}_\epsilon(G) - \widetilde{G}_R) * f\|_{L^p(D)} \leqslant \|\mathcal{R}_\epsilon(G) - \widetilde{G}_R\|_{L^1(D)}\|f\|_{L^p(D)} \leqslant (\|F_{\text{oscill}} - S_{\text{oscill}}\|_{L^1(D)} + \|F_{\text{sing}} - S_{\text{sing}}\|_{L^1(D)})\|f\|_{L^p(D)}.$$

Using spherical coordinates and diam$(D) \leqslant 1$, Proposition 11 yields

$$\|F_{\text{oscill}} - S_{\text{oscill}}\|_{L^1(D)} \leqslant 4\pi\epsilon \int_0^1 (r^2 + r)dr = \frac{20\pi\epsilon}{6}$$

in dimension $d = 3$, and

$$\|F_{\text{oscill}} - S_{\text{oscill}}\|_{L^1(D)} \leqslant 2\pi\epsilon \int_0^1 (r + r^{3/2})dr = \frac{18\pi\epsilon}{10}$$

in dimension $d = 2$. Similarly, but using Proposition 8, we have

$$\|F_{\text{sing}} - S_{\text{sing}}\|_{L^1(D)} \leqslant 4\pi\left(\int_0^{\delta_0} r\,dr + \epsilon \int_{\delta_0}^1 r\,dr\right) \leqslant 2\pi(\delta_0^2 + \epsilon)$$

for $d = 3$, and

$$\|F_{\text{sing}} - S_{\text{sing}}\|_{L^1(D)} \leqslant 2\pi\left(\int_0^{\delta_0} \log\left(1+\frac{1}{r^2}\right)r\,dr + \epsilon\int_{\delta_0}^1 \log\left(1+\frac{1}{r^2}\right)r\,dr\right) \leqslant 2\pi(\delta_0^2\log\delta_0^{-1} + \delta_0^2 + \epsilon(\log 2 + \delta_0^2\log\delta_0^{-1}))$$

for $d = 2$. In dimension $d = 3$ we select $\delta_0 = \sqrt{\epsilon}$; in dimension $d = 2$ we choose δ_0 so that $\epsilon = \delta_0^2 \log\delta_0^{-1}$. With these choices, we combine the estimates and obtain the result. $\square$

5. Quadratures in the Fourier domain

An algorithm to convolve with (28) requires appropriate quadratures to discretize the Fourier integral. Noting that the kernel in (27) is radially symmetric and effectively band-limited, we follow the approach in [11] and develop an algorithm applicable to any kernel of this type. We separate radial and angular variables and, in the radial direction, develop quadratures for exponentials incorporating the kernel as a part of the measure. We describe our approach in dimension $d = 2$ and comment on the extension to dimension $d = 3$ in Remark 16.

Using polar system of coordinates in the Fourier domain, we have

$$(S_{\text{oscill}} * f)(\mathbf{x}) = \frac{1}{4\pi^2} \int_0^{2\pi} \int_0^{b\kappa} \widehat{S}_{\text{oscill}}(\rho)\hat{f}(\rho\cos\theta, \rho\sin\theta)e^{i\rho(x_1\cos\theta + x_2\sin\theta)}\rho\,d\rho\,d\theta, \tag{44}$$

which we approximate as

$$(\widetilde{S}_{\text{oscill}} * f)(\mathbf{x}) = \frac{1}{2\pi} \sum_{j=1}^J \frac{p_j}{L_j} \sum_{l=0}^{L_j-1} \hat{f}(\rho_j\cos\theta_l, \rho_j\sin\theta_l)e^{i\rho_j(x_1\cos\theta_l + x_2\sin\theta_l)}, \tag{45}$$

where

$$\widetilde{S}_{\text{oscill}}(x_1, x_2) = \frac{1}{2\pi} \sum_{j=1}^J \frac{p_j}{L_j} \sum_{l=0}^{L_j-1} e^{i\rho_j(x_1\cos\theta_l + x_2\sin\theta_l)} \tag{46}$$

and the nodes and weights are described below.

Proposition 12. Let $f \in L^p(D), 1 \leqslant p \leqslant \infty$ and consider diam$(D) \leqslant 1$ in dimension $d = 2$. If S_{oscill} is constructed via Proposition 11, then for $\epsilon > 0$ there are quadrature nodes $(\rho_j\cos\theta_l, \rho_j\sin\theta_l)$ and real coefficients p_j in (45) such that

$$\|(S_{\text{oscill}} - \widetilde{S}_{\text{oscill}}) * f\|_{L^p(D)} \leqslant \epsilon\|f\|_{L^p(D)}.$$

Proof. To construct $\widetilde{S}_{\text{oscill}}$ in (46), we follow the approach in [11] and develop a polar grid in the disk of radius $b\kappa$. First, using the algorithm in [25], we construct radial quadratures

$$\left|\int_{-b\kappa}^{b\kappa} \widehat{S}_{\text{oscill}}(|\rho|)e^{i\rho t}|\rho|d\rho - \sum_{j=1}^{J_{\text{diam}}} p_j e^{i\rho_j t}\right| \leqslant \pi\epsilon \quad \text{for } |t| \leqslant 1, \tag{47}$$

where $|\rho_j| \leqslant b\kappa$. The range $|t| \leqslant 1$ follows because $t = (x_1 - y_1)\cos\theta + (x_2 - y_2)\sin\theta$, where $\mathbf{x} = (x_1, x_2), \mathbf{y} = (y_1, y_2)$ for $\mathbf{x}, \mathbf{y} \in D$ and diam$(D) \leqslant 1$. For the angular quadratures, we determine the number of equally spaced angular nodes for each circle of radius ρ_j (see [11, Section 3]), so that

$$\left|\int_0^{2\pi} e^{i\rho_j((x_1-y_1)\cos\theta + (x_2-y_2)\sin\theta)}\,d\theta - \frac{2\pi}{L_j}\sum_{l=0}^{L_j-1} e^{i\rho_j((x_1-y_1)\cos\theta_l + (x_2-y_2)\sin\theta_l)}\right| \leqslant \frac{2\pi^2\epsilon}{\left|\sum_{j=1}^{J_{\text{diam}}} p_j\right|}. \tag{48}$$

Since the radial quadratures in (47) are constructed on the diameter of the disk, using all angles in (48) covers the disk twice. Thus, it is sufficient to use $J = \lfloor(J_{\text{diam}} + 1)/2\rfloor$ radial nodes, where $\lfloor\cdot\rfloor$ denotes the integer part.

Table 2

Number of quadrature nodes, J_{diam}, along the diameter in dimension $d = 2$ (47) and the resulting total number, $N_F = \sum_{j=1}^{J} L_j$, in the disk (49). We have chosen $b = 3, \delta = \epsilon$, and $\alpha^2 = \frac{\log \epsilon^{-1}}{b^2 - 1}$. We observe a weak dependence of the number of nodes on accuracy and effectively linear dependence of J_{diam} on κ for fixed ϵ.

	$\kappa = 25$		$\kappa = 50$		$\kappa = 75$		$\kappa = 100$		$\kappa = 125$		$\kappa = 150$	
	J_{diam}	N_{tot}	J_{diam}	N_{tot}	J_{diam}	N_{tot}	J_{diam}	N_{tot}	J_{diam}	N_{tot}	J_{diam}	N_{tot}
$\epsilon = 10^{-3}$	25	505	49	1935	73	4274	97	7523	121	11677	145	16742
$\epsilon = 10^{-6}$	26	628	50	2240	74	4764	98	8258	122	12670	146	18009
$\epsilon = 10^{-9}$	27	715	51	2429	75	5133	99	8782	123	13366	147	18901
$\epsilon = 10^{-12}$	28	801	52	2636	76	5449	100	9255	124	14005	148	19701

By adding and subtracting $\frac{1}{4\pi^2} \int_0^{2\pi} \sum_{j=1}^{J} p_j e^{i\rho_j((x_1 - y_1)\cos\theta + (x_2 - y_2)\sin\theta)} \, d\theta$, using the triangle inequality, and estimates (47) and (48), we obtain

$$|S_{\text{oscill}}(\mathbf{x} - \mathbf{y}) - \widetilde{S}_{\text{oscill}}(\mathbf{x} - \mathbf{y})| \leqslant \epsilon, \quad \mathbf{x}, \mathbf{y} \in D. \tag{49}$$

Finally, using Minkowski's inequality for convolutions (see e.g. [24, p. 20]), (49), and recalling that $\text{diam}(D) \leqslant 1$, we have

$$\|(S_{\text{oscill}} - \widetilde{S}_{\text{oscill}}) * f\|_{L^p(D)} \leqslant \|S_{\text{oscill}} - \widetilde{S}_{\text{oscill}}\|_{L^1(D)} \|f\|_{L^p(D)} \leqslant \epsilon \cdot \text{diam}(D) \|f\|_{L^p(D)} \leqslant \epsilon \|f\|_{L^p(D)}. \qquad \square$$

We finish this section with several remarks.

Remark 13. Results in [25] indicate that the number of nodes in (47) is $J_{\text{diam}} \sim b\kappa + c_1 \log b\kappa + c_2 \log \epsilon^{-1}$. As described in [11, Section 3.2], the number of angular nodes on the largest radius is $L_J \sim b\kappa + c_3 \log \epsilon^{-1}$, where c_1, c_2 and c_3 are constants. Thus, the total number of quadrature nodes in the Fourier domain may be estimated as $N_F \sim (b\kappa)^2 + c_0 (\log \epsilon^{-1})^2$, where c_0 is a constant. We note that the number of terms in (27) does not affect the final number of quadrature nodes since all these terms are accounted for by the quadrature weights. We display the number of quadrature nodes as a function of ϵ and κ in Table 2.

Remark 14. Although $\widehat{S}_{\text{oscill}}(|\rho|)|\rho|$ in (47) is not sign definite, we interpret the approximation in (47) as a quadrature (see [25]). Furthermore, since $\widehat{S}_{\text{oscill}}$ is a smooth function, we integrate across $\rho = \kappa$ with no difficulty. In Fig. 3, we provide an example of the quadratures in (47) and note the symmetry of the nodes $\rho_{J_{\text{diam}} - j + 1} = -\rho_j$ and weights $p_{J_{\text{diam}} - j + 1} = p_j$.

Remark 15. To convolve with the imaginary part of Green's function,

$$(\mathcal{I}m(G) * f)(\mathbf{x}) = \frac{1}{8\pi} \int_0^{2\pi} \hat{f}(\kappa \cos\theta, \kappa \sin\theta) e^{i\kappa(x_1 \cos\theta + x_2 \sin\theta)} \, d\theta,$$

we use the angular discretization described in (48) to obtain the approximation

$$(\widetilde{G}_I * f)(\mathbf{x}) = \frac{1}{8\pi} \sum_{l=0}^{L_\kappa - 1} \hat{f}(\kappa \cos\theta_l, \kappa \sin\theta_l) e^{i\kappa(x_1 \cos\theta_l + x_2 \sin\theta_l)}, \tag{50}$$

so that

$$\|(\mathcal{I}m(G) - \widetilde{G}_I) * f\|_{L^p(D)} \leqslant \epsilon \|f\|_{L^p(D)}. \tag{51}$$

Remark 16. In dimension $d = 3$, instead of (47) we use the construction in [25] to approximate

$$\left| \int_{-b\kappa}^{b\kappa} \widehat{S}_{\text{oscill}}(|\rho|) e^{i\rho t} \rho^2 \, d\rho - \sum_{j=1}^{J_{\text{diam}}} p_j e^{i\rho_j t} \right| \leqslant \pi^2 \epsilon \tag{52}$$

for $|t| \leqslant 1$ (see Table 3 displaying J_{diam} as a function of ϵ and κ). The angular discretization of the circle should be replaced by that of the sphere.

6. Algorithm for computing convolutions with Green's function

Let us describe an algorithm for computing convolutions with Green's function

$$u(\mathbf{x}) = \int_D G(\mathbf{x} - \mathbf{y}) f(\mathbf{y}) d\mathbf{y}$$

in dimension $d = 2, 3$, and estimate its complexity. We refer to f and u as the input and output functions. We first assume that the input function and its Fourier transform (within a disk of radius proportional to κ) are given, and we are free to
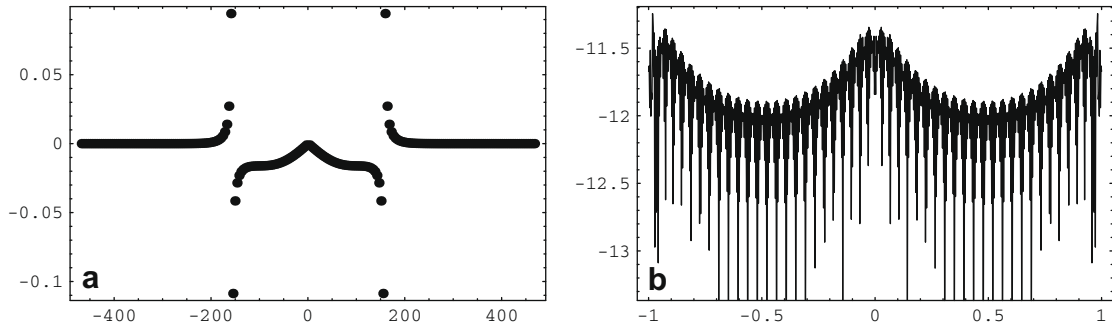
Fig. 3. (a) Weights vs. nodes of the radial quadrature (47) in dimension $d = 2$ with $\kappa = 50\pi$ and $b = 3$. (b) Absolute error in (47) using $\log_{10}$ scale on the vertical axis.

Table 3
Number of quadrature nodes, J_{diam}, along the diameter in dimension $d = 3$ (52). We have chosen $b = 3, \delta = \epsilon$, and $\alpha^2 = \frac{\log \epsilon^{-1}}{b^2 - 1}$. Note that these numbers are almost the same as those in Table 2.

	$\kappa = 25$	$\kappa = 50$	$\kappa = 75$	$\kappa = 100$	$\kappa = 125$	$\kappa = 150$
$\epsilon = 10^{-3}$	27	51	75	99	123	147
$\epsilon = 10^{-6}$	28	52	76	100	124	148
$\epsilon = 10^{-9}$	29	53	77	101	125	149
$\epsilon = 10^{-12}$	30	54	78	102	126	150

discretize them as needed. We note that the cost associated with computing the band-limited Fourier transform is described below and does not change the overall complexity of the algorithm.

Initialization:

(1) *Fourier domain initialization*: For fixed κ and given accuracy ϵ, we select b (which ultimately determines α in (37)) and construct $\widetilde{S}_{\text{oscill}}$ using the N_F-point quadrature given in (46), $N_F = \sum_{j=1}^{J} L_j$ (or its analogue in dimension $d = 3$, see Remark 16). We estimate the number of nodes as $N_F \sim (b\kappa)^d + C_0(\log \epsilon^{-1})^d$, where C_0 is a constant (see Remark 13 and Tables 2 and 3 for illustration).

(2) *Spatial domain initialization*: For fixed κ and given accuracy ϵ, we construct S_{sing} as a Gaussian representation in (26) with N terms, where a conservative estimate yields $N \sim (\log \epsilon^{-1})^2$ (in practice we observe $N \sim \log \epsilon^{-1}$, see Table 1). We note that the number of terms N depends weakly on κ, with N decaying as κ grows and S_{sing} becomes more localized.

(3) *Discretization of the input function*: We use the multiresolution algorithm in [7] to adaptively discretize the input function with a tensor product basis having p scaling functions per dimension. If N_{box} is the total number of boxes used to represent the input function with accuracy ϵ, then the total number of input points is $N_{\text{in}} = N_{\text{box}}p^d$. In practical applications we choose $p \sim \log \epsilon^{-1}$ since it improves the overall performance. Thus, we have $N_{\text{in}} \sim N_{\text{box}}(\log \epsilon^{-1})^d$. We note that it is not hard to construct examples of functions for which an adaptive representation offers no advantage; in such case the number of points is $N_{\text{in}} \sim \kappa^d$ due to the required Nyquist sampling rate. Thus, in the worst case, we have $N_{\text{in}} \sim \kappa^d + C_1(\log \epsilon^{-1})^d$.

(4) *Initialization of the output function*: The output function, a sum of spatial and Fourier contributions, is evaluated on a user chosen set of N_{out} points. While the spatial contribution may retain an adaptive structure if we use the algorithm from [7], the Fourier contribution results in $\mathcal{O}(\kappa^d)$ points due to the required Nyquist sampling rate. Thus, unless there are special circumstances, $N_{\text{out}} \sim \kappa^d$. Again, in the worst case we have $N_{\text{out}} \sim \kappa^d + C_2(\log \epsilon^{-1})^d$.

Application of the operator:

(1) *Convolution with S_{sing}*: Using the algorithm in [7], the complexity of applying S_{sing} is $\mathcal{O}(p \cdot N \cdot N_{\text{in}})$. Alternatively, the fast Gauss transform (see [8–10]) may be used and results in a similar computational complexity. Although $p \cdot N$ is formally estimated as $p \cdot N \sim (\log \epsilon^{-1})^3$, we note that within the range of parameters we experimented with, this factor behaves effectively as a constant (the over estimation is, in part, due to the fact that the algorithm in [7] does not use all Gaussian terms on all scales). With this caveat, the computational complexity of this step is $\mathcal{O}(\kappa^d + C_3(\log \epsilon^{-1})^d)$, where C_3 is a constant.

(2) *Convolution with $\widetilde{S}_{\text{oscill}}$ and $\mathcal{I}_{m}(G)$*: We evaluate the Fourier transform of the input function $\hat{f}$ at the quadrature nodes (49) and (51). Then, given the node locations for the output function, u, we use the USFFT [12–14] to evaluate the trigonometric sums (45) and (51) (or their analogue for dimension $d = 3$, see remark above). Thus, the computational complexity of applying $\widetilde{S}_{\text{oscill}}$ and $\mathcal{I}_{m}(G)$ is $\mathcal{O}(N_{\text{out}} + N_F) + \mathcal{O}(\kappa^d \log \kappa)$, or $\mathcal{O}(\kappa^d \log \kappa + C_4(\log \epsilon^{-1})^d)$, where C_4 is a constant.

The assumption that the band-limited Fourier transform of the input function is available does not change the overall complexity of the algorithm (even for functions with discontinuities or singularities). Due to the band-limiting nature of $\widetilde{S}_{\text{oscill}}$ (as well as of $\mathcal{I}m(G)$), we only need to compute the Fourier transform of the input function within a ball of radius $b\kappa$. Using the USFFT [12–14] (which, in fact, was designed for this purpose), the computational cost scales at most as $\mathcal{O}((\log \epsilon^{-1})^d \kappa^d \log \kappa)$. For example, the algorithm in [12] first projects the function onto a subspace of splines where the number of splines is proportional to $(\kappa \log \epsilon^{-1})^d$. This step is followed by the FFT requiring $\mathcal{O}(\kappa^d \log \kappa)$ operations and the final adjustment of the computed values involving $\mathcal{O}(\kappa^d)$ operations. Since a typical implementation of USFFT fixes the accuracy, e.g. double precision, we estimate the overall cost of computing the band-limited Fourier transform as dependent only on κ.

The performance of both, the spatial and Fourier components of our method, have been examined in the references mentioned above. We note that in many practical instances the semi-analytic nature of our approximation may allow for additional savings.

6.1. Examples

We start by applying the operator to a delta function in dimension $d = 2$. The motivation for presenting this example is twofold: (i) to demonstrate that our approach is accurate for functions which do not decay in the Fourier domain and (ii) to illustrate both parts of the approximation, S_{sing} (26) and $\widetilde{S}_{\text{oscill}}$ (46).

In Fig. 4, we plot the result of convolving with S_{sing} and $\widetilde{S}_{\text{oscill}}$ for different values of b. Fig. 4(b) and (d) demonstrates that the spatial part S_{sing} is well localized and captures the singularity at $r = 0$ of Green's function (14). Also, as seen in Fig. 4(a) and (c), the Fourier part $\widetilde{S}_{\text{oscill}}$ captures the oscillations of Green's function. We note that the spike centered at zero in Fig. 4(a) is larger than that in Fig. 4(c) due to the choice of parameter b (see Proposition 5 and Fig. 1). In Fig. 5, we plot the absolute error of our approximation as a function of radius. We note that the error behaves better than the estimates obtained in Theorem 1.
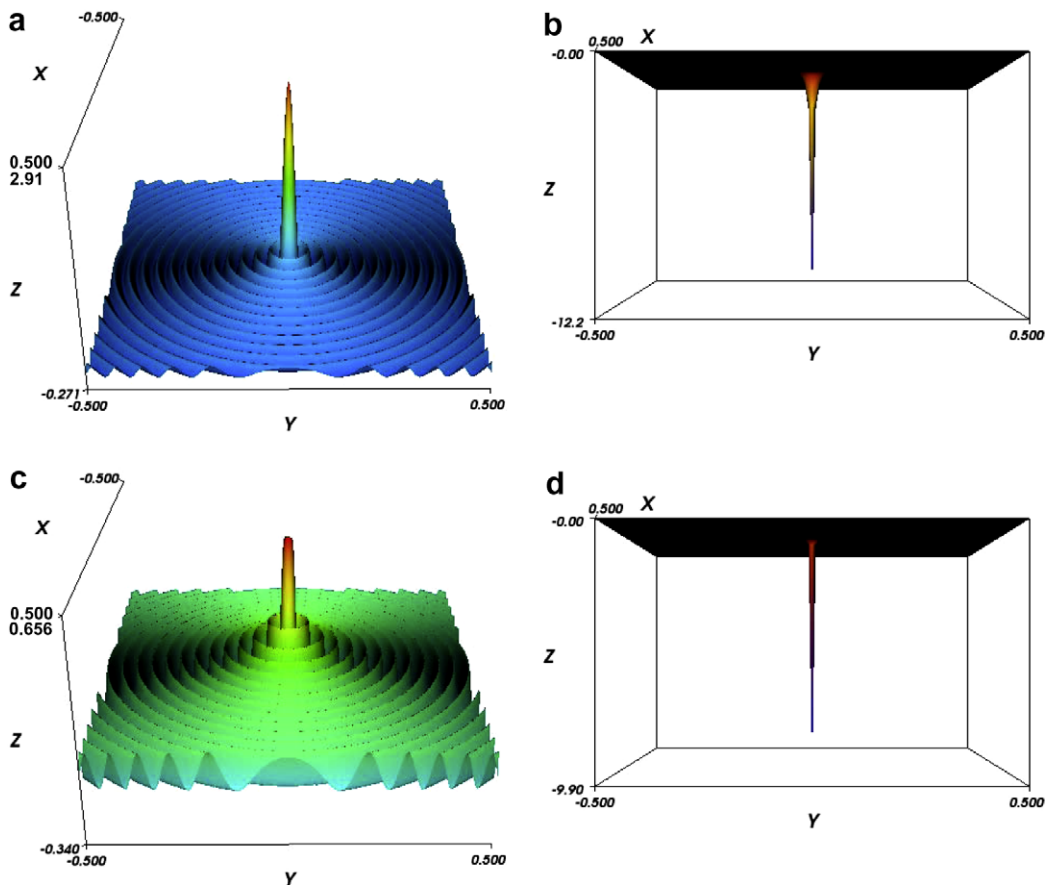

Fig. 4. Result of applying the Helmholtz operator in dimension $d = 2$ with $\kappa = 50\pi$ to a delta function, thus displaying the kernel (in the spatial domain). The sum of $\widetilde{S}_{\text{oscill}}$ and S_{sing} approximates the real part of Green's function. Figures (a) and (c) display $\widetilde{S}_{\text{oscill}}$ (46) for $b = 3$ and $b = 5$, (respectively) and Figures (b) and (d) S_{sing} (26) for $b = 3$ and $b = 5$.
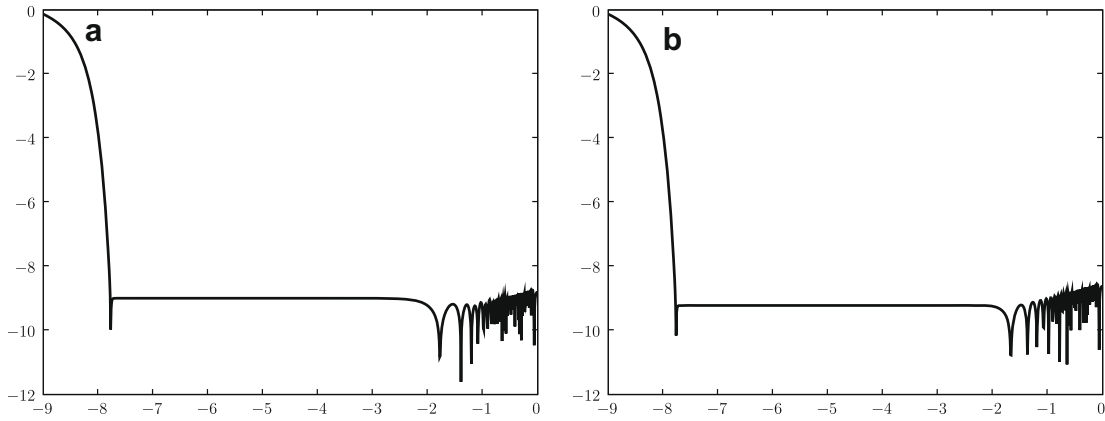
Fig. 5. Absolute error (as a function of radius using $\log_{10} - \log_{10}$ scale) of approximating the real part of Green's function with $\kappa = 50\pi$ and $\delta_0 \approx 10^{-8}$ for parameter (a) $b = 3$ and (b) $b = 5$.

Next we verify the accuracy of applying Green's function to the discontinuous function:

$$f(\mathbf{x}) = \begin{cases} a, & |\mathbf{x}| \leqslant r_f, \\ 0, & |\mathbf{x}| > r_f \end{cases} \tag{53}$$

with $a \in \mathbb{R}$ and $r_f > 0$. For this f, the solution to (4) in dimension $d = 2$ satisfying the Sommerfeld condition is given by

$$u(\mathbf{x}) = \begin{cases} \frac{a}{\kappa^2}(1 + c_1 J_0(\kappa|\mathbf{x}|)), & |\mathbf{x}| \leqslant r_f, \\ c_2 \frac{a}{\kappa^2} H_0^{(1)}(\kappa|\mathbf{x}|), & |\mathbf{x}| > r_f, \end{cases} \tag{54}$$

where

$$c_1 = \frac{i H_1^{(1)}(r_f \kappa)}{J_1(r_f \kappa) Y_0(r_f \kappa) - J_0(r_f \kappa) Y_1(r_f \kappa)}$$

and

$$c_2 = -\frac{i J_1(r_f \kappa)}{J_1(r_f \kappa) Y_0(r_f \kappa) - J_0(r_f \kappa) Y_1(r_f \kappa)}$$

are selected to assure $u \in C^1(\mathbb{R}^2)$. We apply to f our approximation of the two-dimensional Green's function, so that we can compare the result with the exact solution u in (54). We choose this example because $\hat{f}(\rho)$ has slow decay ($\hat{f} \sim 1/\rho^{3/2}$) and, thus, tests both the spatial and the Fourier parts of the algorithm. In our example we consider Green's function with $\kappa = 50\pi$ and f with $r_f = 1/5$ and $a = \kappa^2$. We choose $\epsilon \approx 10^{-9}$ and $b = 3$ (as in Fig. 5(a)) and construct S_{sing} in (26) and $\widetilde{S}_{\text{oscill}}$ in (46). It is important to note that the L^∞-norm of the solution is $\|u\|_\infty \approx 6.35$, whereas that of the input function is $\|f\|_\infty = \kappa^2 \approx 2.47 \cdot 10^5$. Since the purpose of our test is to demonstrate the accuracy of applying the approximate Green's function, we convolve S_{sing} with f in (53) directly (as a one-dimensional integral) and use the product of $\widetilde{S}_{\text{oscill}}$ and $\hat{f}(\rho)$ in the Fourier domain.

In Fig. 6, we display the absolute error of the real and imaginary parts plotted along the diagonal of the unit box. Since $f \approx 10^5$ for $|\mathbf{x}| \leqslant r_f$, we expect the absolute error of the real part to be five orders of magnitude larger than in the region $|\mathbf{x}| > r_f$. The absolute error in Fig. 6(a) agrees with the relative error estimate in Theorem 2 if the norm of the input function is taken into account. The absolute error due to approximation of the imaginary part of Green's function is much better than predicted by the estimate in (51). This is due to the exponential decay of the error in using the trapezoidal rule (see Fig. 6(b)).

Achieving a target absolute error for the output function requires an approximation of Green's function that takes into account the norm of the input function. However, even if this norm is large, the additional computational cost it implies is minimal because the complexity of our algorithm scales logarithmically with accuracy.

We also provide an example as an illustration, where we convolve Green's function with a fairly complicated function with jump discontinuities, see Fig. 7.

Finally, we tabulate the number of quadrature nodes required to construct S_{sing} in (26) and $\widetilde{S}_{\text{oscill}}$ in (46) as a function of the desired accuracy ϵ and parameter κ. This provides numerical evidence for claims made in Remark 13.

In Table 1, we display the number of Gaussian terms in S_{sing} (26) for dimension $d = 3$ using the quadratures associated with the PSWFs [25]. This table shows that for fixed κ and within the range of considered parameters, the number of Gaussians behaves more as $N(\epsilon) \sim \log \epsilon^{-1}$ rather than $N(\epsilon) \sim (\log \epsilon^{-1})^2$ as in the estimates in [3, Appendix A]. We note that as κ grows, $\widetilde{S}_{\text{oscill}}$ accounts for a larger volume in the Fourier domain and, thus, S_{sing} requires fewer Gaussians as is reflected in Table 1.

In Table 2, we display the number of quadrature nodes in the Fourier domain (in dimension $d = 2$) along the diameter (47) and their total number within the disk of radius $b\kappa$ (49). For fixed ϵ, we observe that $J_{\text{diam}} \sim \kappa$ and $N_F \sim \kappa^2$. This result
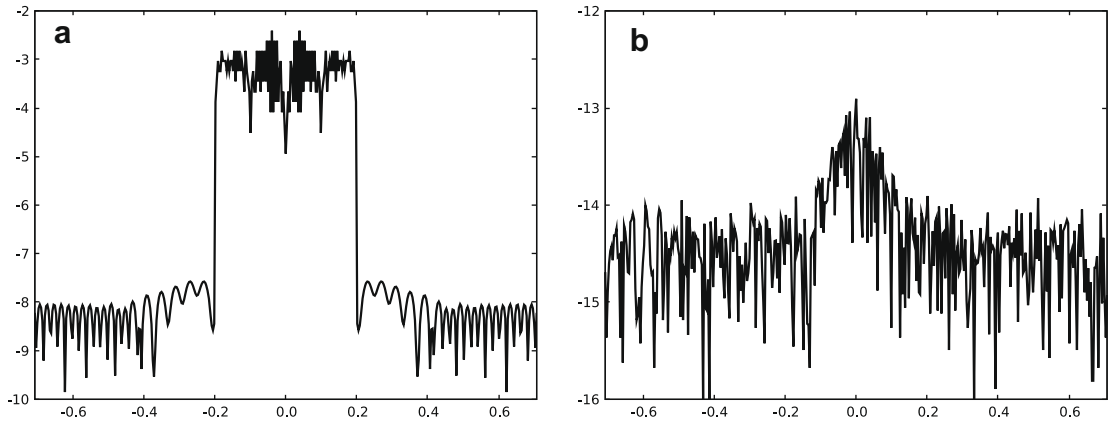
Fig. 6. For f in (53), we display (a) real part and (b) imaginary part of the absolute error of the computed solution (4) satisfying the Sommerfeld condition. The error is plotted along the unit box diagonal using $\log_{10}$ scale on the vertical axis. Green's function was constructed with parameters from Fig. 5a. Note that Theorem 2 only assures the relative error and in this example $\|f\|_\infty \approx 10^5$.
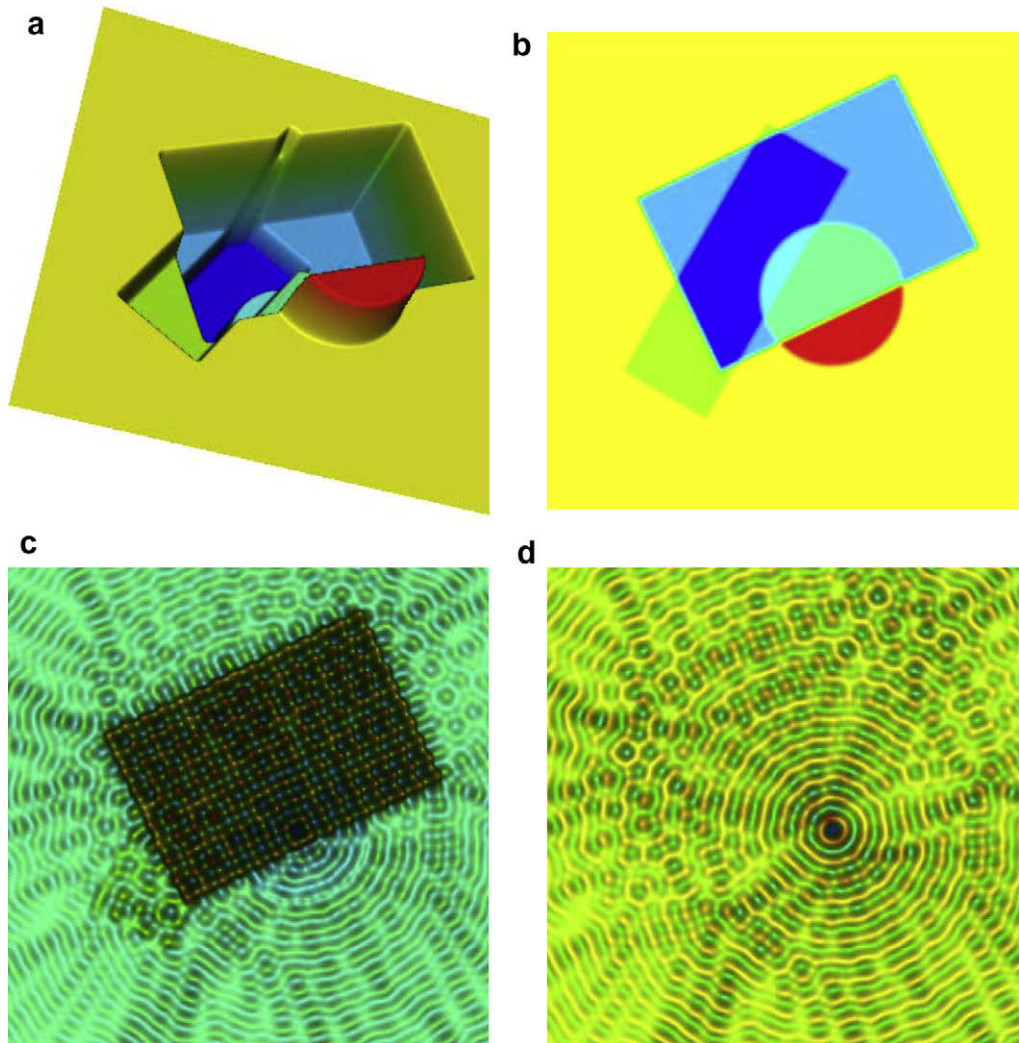

Fig. 7. Convolution with Green's function ($\kappa = 50\pi$), where the different views of the function are shown in Figures (a) and (b). We display the real part (c) and imaginary part (d) of the result.

is expected as the number of nodes in this construction approaches optimal (i.e., effectively approaches $b\kappa/\pi$) as κ gets large. For fixed κ, we observe J_{diam} depends weakly on ϵ and, thus, effectively $N_F \sim \log \epsilon^{-1}$ rather than $N_F \sim (\log \epsilon^{-1})^2$ obtained by estimates.

In Table 3, we display the number of radial quadrature nodes in the Fourier domain along the diameter in dimension $d = 3$ in (52). We note that the number of quadrature nodes along the diameter in dimensions $d = 2$ and $d = 3$ are almost the same.

7. Conclusion and remarks

We develop an approximation of the free space Helmholtz Green's function in dimensions $d = 2, 3$ by splitting its action between the spatial and Fourier domains. Our approximation achieves:

- a spatial domain representation as a sum of Gaussians, capturing the singularity of Green's function at zero, and
- a Fourier domain representation as a smooth, radially symmetric and effectively band-limited kernel.

Using properties of this approximation, we construct a fast and accurate algorithm for computing convolutions with Green's function and illustrate its performance in dimension $d = 2$. We indicate how to extend the algorithm (specifically, by using a discretization of a sphere in the Fourier domain) to dimension $d = 3$. We expect our approach to be most useful for accurate computations in problems where the media or potentials are described by functions with discontinuities or singularities.

The extension of our approach to the Helmholtz Green's function with periodic or Dirichlet/Neumann boundary conditions may be found in [2].

Acknowledgment

Appendix A. *A.1. Proof of regularization*

Since $1/(\rho^2 - (\kappa \pm i\lambda)^2)$ is radially symmetric, we apply (9) and (10).
In dimension $d = 3$, using [30, 3.723 (3)], we have

$$\lim_{\lambda \to 0^+} \frac{1}{|\mathbf{x}|^{\frac{1}{2}}(2\pi)^{\frac{3}{2}}} \int_0^\infty \frac{\rho^{\frac{3}{2}} J_{\frac{1}{2}}(|\mathbf{x}|\rho)}{\rho^2 - (\kappa \pm i\lambda)^2} d\rho = \lim_{\lambda \to 0^+} \frac{1}{2\pi^2|\mathbf{x}|} \int_0^\infty \frac{\rho \sin \rho|\mathbf{x}|}{\rho^2 - (\kappa \pm i\lambda)^2} d\rho = \frac{1}{4\pi} \frac{e^{\pm i\kappa|\mathbf{x}|}}{|\mathbf{x}|}.$$

In dimension $d = 2$, using [30, 6.532 (4), 28, 9.6.4], we obtain

$$\lim_{\lambda \to 0^+} \frac{1}{2\pi} \int_0^\infty \frac{\rho J_0(|\mathbf{x}|\rho)}{\rho^2 - (\kappa \pm i\lambda)^2} d\rho = \frac{1}{2\pi} K_0(\mp i\kappa|\mathbf{x}|) = \frac{i}{4} H_0^{(1)}(\pm\kappa|\mathbf{x}|),$$

where $H_0^{(1)}$ is the zeroth order Hankel function of the first kind.

A.2. Proof of Proposition 5

Proof. The proof combines the estimates from Lemmas 17 and 18. Because of the assumption on α,

$$e^{-\alpha^2(b^2-1)} = \delta$$

and since $b \geqslant \sqrt{2}$ and $\delta \leqslant 1/3$ we have

$$\delta e^{2\alpha^2\delta} = \delta \delta^{-\frac{2\delta}{b^2-1}} \leqslant \delta \delta^{-\delta} \leqslant 2\delta. \tag{55}$$

For $d = 3$ we obtain

$$|F_{\mathrm{oscill}}(r) - I_-(r) - I_{+,b}(r)| \leqslant \frac{\delta e^{2\alpha^2\delta}}{2\pi^2}(6 + 9\alpha^2) + \frac{e^{-\alpha^2(b^2-1)}}{4\pi^2 r \alpha^2(b^2-1)} \leqslant \frac{6\delta}{\pi^2} + \frac{9\delta \log \delta^{-1}}{\pi^2(b^2-1)} + \frac{\delta}{4\pi^2 r \log \delta^{-1}} \leqslant \delta \log \delta^{-1}\left(2 + \frac{1}{r}\right),$$

where we again used the assumptions on b, α, and $\log \delta^{-1} > 1$.
Similarly for $d = 2$ we have

$$|F_{\mathrm{oscill}}(r) - I_-(r) - I_{+,b}(r)| \leqslant \frac{\delta e^{2\alpha^2\delta}}{2\pi}\left(\sqrt{6r} + 6\alpha^2 + \frac{8}{3}\right) + \frac{e^{-\alpha^2(b^2-1)}}{4\pi\alpha^2(b^2-1)} \leqslant \frac{\sqrt{6}\sqrt{r}\delta}{\pi} + \frac{6\delta \log \delta^{-1}}{\pi} + \frac{8\delta}{3\pi} + \frac{\delta}{4\pi \log \delta^{-1}}$$

$$\leqslant \delta \log \delta^{-1}\left(3 + \sqrt{r}\right). \quad \square$$

A.3. Proof of Proposition 8

Proof. We begin by truncating the region of integration in (25) to the interval $[-\log(\alpha/\kappa), \gamma]$ where γ will be chosen later. We claim that there exists a N-term quadrature with nodes x_n and weights $\omega_n > 0$ (see e.g. the generalized Gaussian quadratures in [25, Section 7]), such that in dimension $d = 3$ we have

$$\left| \frac{1}{4\pi^{3/2}} \int_{-\log\frac{2}{\kappa}}^{\gamma} e^{-r^2\frac{e^{2s}}{4}} e^{\kappa^2 e^{-2s} + s} \, ds - \sum_{n=1}^{N} q_n e^{-\sigma_n r^2} \right| \leqslant \frac{\epsilon}{2r} \tag{56}$$

for $0 \leqslant r < \infty$, where $q_n = \omega_n e^{\kappa^2 e^{-2x_n} + x_n}/4\pi^{3/2}$ and $\sigma_n = e^{2x_n}/4$. Using the definition of F_{sing} (25), and noting that the integrand is positive, we have

$$\left| F_{\text{sing}}(r) - \sum_{n=1}^{N} q_n e^{-\sigma_n r^2} \right| \leqslant \frac{\epsilon}{2r} + \frac{1}{4\pi^{3/2}} \int_{\gamma}^{\infty} e^{-r^2\frac{e^{2s}}{4}} e^{\kappa^2 e^{-2s} + s} \, ds. \tag{57}$$

Using the change of variable $t = r^2 e^{2s}/4$, and estimating $e^{\kappa^2 e^{-2s}}$ by its upper bound, we have

$$I(d) = \frac{1}{2^{d-1}\pi^{d/2}} \int_{\gamma}^{\infty} e^{-r^2\frac{e^{2s}}{4}} e^{\kappa^2 e^{-2s} + (d-2)s} \, ds \leqslant \frac{e^{\kappa^2 e^{-2\gamma}}}{4\pi^{d/2} r^{d-2}} \Gamma\left(\frac{d}{2} - 1, \left(\frac{e^{\gamma} r}{2}\right)^2\right), \tag{58}$$

where $\Gamma(\cdot, \cdot)$ is the incomplete Gamma function see e.g. [28, 6.5.3]. Using [28, 6.5.17],

$$I(3) \leqslant \frac{e^{\kappa^2 e^{-2\gamma}}}{4\pi r} \left(1 - \text{erf}\left(\frac{e^{\gamma} r}{2}\right)\right),$$

we select γ sufficiently large so that

$$\frac{e^{\kappa^2 e^{-2\gamma}}}{4\pi r} \left(1 - \text{erf}\left(\frac{e^{\gamma} r}{2}\right)\right) \leqslant \begin{cases} \frac{1}{2r} & \text{for } 0 \leqslant r < \delta_0, \\ \frac{\epsilon}{2r} & \text{for } r \geqslant \delta_0. \end{cases} \tag{59}$$

We use $\epsilon \leqslant 1$, (59) and (57) to obtain (38).

Similarly in dimension $d = 2$, we construct a quadrature

$$\left| \frac{1}{2\pi} \int_{-\log\frac{2}{\kappa}}^{\gamma} e^{-r^2\frac{e^{2s}}{4}} e^{\kappa^2 e^{-2s}} \, ds - \sum_{n=1}^{N} q_n e^{-\sigma_n r^2} \right| \leqslant \frac{\epsilon}{2} \log\left(1 + \frac{1}{r^2}\right) \tag{60}$$

for $0 \leqslant r < \infty$, where $q_n = \omega_n e^{\kappa^2 e^{-2x_n}}/2\pi$ and $\sigma_n = e^{2x_n}/4$. Instead of (57) we have

$$\left| F_{\text{sing}}(r) - \sum_{n=1}^{N} q_n e^{-\sigma_n r^2} \right| \leqslant \frac{\epsilon}{2} \log\left(1 + \frac{1}{r^2}\right) + \frac{1}{2\pi} \int_{\gamma}^{\infty} e^{-r^2\frac{e^{2s}}{4}} e^{\kappa^2 e^{-2s}} \, ds. \tag{61}$$

Using (58) and [28, 6.5.15, 5.1.20] we have

$$I(2) \leqslant \frac{1}{4\pi} e^{\kappa^2 e^{-2\gamma}} E_1\left(\frac{e^{2\gamma} r^2}{4}\right) \leqslant \frac{1}{4\pi} e^{\kappa^2 e^{-2\gamma}} e^{-\frac{e^{2\gamma} r^2}{4}} \log\left(1 + \frac{4}{e^{2\gamma} r^2}\right),$$

where E_1 is the Exponential Integral [28, 5.1.1]. Selecting γ sufficiently large, we have

$$\frac{1}{4\pi} e^{\kappa^2 e^{-2\gamma}} e^{-\frac{e^{2\gamma} r^2}{4}} \log\left(1 + \frac{4}{e^{2\gamma} r^2}\right) \leqslant \begin{cases} \frac{1}{2} \log\left(1 + \frac{1}{r^2}\right) & \text{for } 0 \leqslant r < \delta_0, \\ \frac{\epsilon}{2} \log\left(1 + \frac{1}{r^2}\right) & \text{for } r \geqslant \delta_0. \end{cases} \tag{62}$$

We use $\epsilon \leqslant 1, \delta_0 \leqslant 1$, (62) and (61) to obtain (39). $\square$

A.4. Proof of Proposition 10

Proof. We let $\mu = \min\{\kappa\delta, \delta\}$ and use Lemma 19 with $\tilde{\delta} = \mu/(\kappa(b+1))$ to obtain

$$\left| \frac{1}{p^2} - \sum_{m=1}^{M} \tilde{w}_m e^{-\tilde{\tau}_m p^2} \right| \leqslant \frac{\epsilon_0}{p^2}$$

for $p \in [\tilde{\delta}, 1]$. Substituting $p = (\rho \pm \kappa)/(\kappa(b+1))$ and using $b > 1$ and $\delta < 1$ we have

$$\left| \frac{1}{(\rho - \kappa)^2} - \sum_{m=1}^{M} w_m e^{-\tau_m (\rho - \kappa)^2} \right| \leqslant \frac{\epsilon_0}{(\rho - \kappa)^2} \tag{63}$$

for $\rho \in [0, \kappa - \mu] \cup [\kappa + \mu, \kappa b]$ and

$$\left| \frac{1}{(\rho + \kappa)^2} - \sum_{m=1}^{M} w_m e^{-\tau_m (\rho + \kappa)^2} \right| \leqslant \frac{\epsilon_0}{(\rho + \kappa)^2} \tag{64}$$

for $\rho \in [0, b\kappa]$, where

$$w_m = \frac{\tilde{w}_m}{(\kappa(b+1))^2} \tag{65}$$

and

$$\tau_m = \frac{\tilde{\tau}_m}{(\kappa(b+1))^2}. \tag{66}$$

Multiplying (63) by $\rho - \kappa$ for $\rho > \kappa$ and $\kappa - \rho$ for $\rho < \kappa$ and multiplying (64) by $\rho + \kappa$, we have

$$\left| \frac{1}{\rho^2 - \kappa^2} - \frac{1}{2\rho} \sum_{m=1}^{M} w_m ((\rho - \kappa) e^{-\tau_m(\rho-\kappa)^2} + (\rho + \kappa) e^{-\tau_m(\rho+\kappa)^2}) \right| \leqslant \frac{\epsilon_0}{2\rho} \left(\frac{|\rho - \kappa|}{(\rho - \kappa)^2} + \frac{\rho + \kappa}{(\rho + \kappa)^2} \right)$$

for $\rho \in [0, \kappa - \mu] \cup [\kappa + \mu, b\kappa]$. Multiplying by $e^{-\alpha^2(\rho^2 - \kappa^2)/\kappa^2}$ we attain (40) and (41). Finally, since $\epsilon_0 \leqslant 1$, multiplying (64) by $\rho + \kappa$ we obtain (42) and (43) follows from (85). $\quad \square$

A.5. Proof of Proposition 11

Proof. In order to use (28) and (29), we first estimate the difference $\widehat{S}_{\text{oscill}} - \widehat{F}_{\text{oscill}}$ in the regions $\rho \in [0, \kappa - \mu]$ and $\rho \in [\kappa + \mu, b\kappa]$, where $\mu = \min\{\kappa\delta, \delta\}$. As a second step, we estimate the Fourier integral of $\widehat{S}_{\text{oscill}}$ in the region $\rho \in [\kappa - \mu, \kappa + \mu]$ and use Proposition 5 to estimate $\widehat{F}_{\text{oscill}}$ in the regions $\rho \in [\kappa - \mu, \kappa + \mu]$ and $\rho \in [b\kappa, \infty)$.

We first prove the proposition for $d = 3$ and then point out how to approach the $d = 2$ case. We estimate

$$|S_{\text{oscill}}(r) - F_{\text{oscill}}(r)| \leqslant I_1(r) + I_2(r) + I_3(r) + I_4(r),$$

where

$$I_1(r) = \frac{1}{2\pi^2 r} \int_0^{\kappa - \mu} |\widehat{S}_{\text{oscill}}(\rho) - \widehat{F}_{\text{oscill}}(\rho)| |\sin(\rho r)| \rho \, d\rho, \tag{67}$$

$$I_2(r) = \frac{1}{2\pi^2 r} \int_{\kappa + \mu}^{b\kappa} |\widehat{S}_{\text{oscill}}(\rho) - \widehat{F}_{\text{oscill}}(\rho)| |\sin(\rho r)| \rho \, d\rho, \tag{68}$$

$$I_3(r) = \frac{1}{2\pi^2 r} \left| \int_{\kappa - \mu}^{\kappa + \mu} \widehat{S}_{\text{oscill}}(\rho) \sin(\rho r) \rho \, d\rho \right|, \tag{69}$$

$$I_4(r) = \frac{1}{2\pi^2 r} \left| \text{p.v.} \int_{\kappa - \mu}^{\kappa + \mu} \widehat{F}_{\text{oscill}}(\rho) \sin(\rho r) \rho \, d\rho + \int_{b\kappa}^{\infty} \widehat{F}_{\text{oscill}}(\rho) \sin(\rho r) \rho \, d\rho \right|. \tag{70}$$

Using (40), $e^{-\alpha^2 \rho^2 / \kappa^2} \leqslant 1, |\sin(\rho r)| \leqslant 1$, and the definitions of ϵ_0 and c, we have

$$I_1(r) \leqslant \frac{\epsilon_0 e^{\alpha^2}}{4\pi^2 r} \int_0^{\kappa - \mu} \frac{2\kappa}{\kappa^2 - \rho^2} d\rho = \frac{\epsilon_0 e^{\alpha^2}}{4\pi^2 r} \log \frac{2\kappa - \mu}{\mu} \leqslant \frac{\epsilon_0 e^{\alpha^2}}{4\pi^2 r} \log(2 \max\{\kappa, 1\} \delta^{-1})$$

$$\leqslant \frac{\epsilon_0 e^{\alpha^2}}{4\pi^2 r} \log(c\delta^{-1}) = \frac{\delta}{4\pi^2 r} \log(c\delta^{-1}) \tag{71}$$

and, using (41) and our definition of c,

$$I_2(r) \leqslant \frac{\epsilon_0}{4\pi^2 r} \int_{\kappa + \mu}^{b\kappa} \frac{2\rho}{\rho^2 - \kappa^2} d\rho = \frac{\epsilon_0}{4\pi^2 r} \log \frac{\kappa^2(b^2 - 1)}{\mu(\mu + 2\kappa)} \leqslant \frac{\epsilon_0}{4\pi^2 r} \log \left(\frac{\max\{\kappa, 1\}(b^2 - 1)\delta^{-1}}{2} \right) = \frac{\epsilon_0}{4\pi^2 r} \log(c\delta^{-1})$$

$$\leqslant \frac{\delta}{4\pi^2 r} \log(c\delta^{-1}). \tag{72}$$

To estimate (69), we split it into two terms and, in the first term, change variables $q = \rho - \kappa$ so that

$$|I_3(r)| \leqslant \left| \int_{-\mu}^{\mu} \sum_{m=1}^{M} w_m q e^{-\tau_m q^2} f(q+\kappa) dq \right| + \left| \int_{\kappa-\mu}^{\kappa+\mu} \sum_{m=1}^{M} w_m (\rho+\kappa) e^{-\tau_m(\rho+\kappa)^2} f(\rho) d\rho \right|, \qquad (73)$$

where

$$f(\rho) = \frac{1}{4\pi^2 r} e^{-\alpha^2(\rho^2-\kappa^2)/\kappa^2} \sin(\rho r).$$

For the first term in (73) we use Lemma 20 and (43) to obtain

$$\left| \int_{-\mu}^{\mu} \sum_{m=1}^{M} w_m q e^{-\tau_m q^2} f(q+\kappa) dq \right| \leqslant \max_{q \in [-\mu,\mu]} |f'(q+\kappa)| \int_{-\mu}^{\mu} \sum_{m=1}^{M} w_m q^2 e^{-\tau_m q^2} dq \leqslant 4\mu \max_{\rho \in [\kappa-\mu,\kappa+\mu]} |f'(\rho)|. \qquad (74)$$

Using $|\sin(\rho r)/r| \leqslant \rho$ and $(\kappa+\mu)^2/\kappa^2 \leqslant 9/4$, we have

$$\max_{\rho \in [\kappa-\mu,\kappa+\mu]} |f'(\rho)| = \max_{\rho \in [\kappa-\mu,\kappa+\mu]} \left| \frac{e^{-\alpha^2(\rho^2-\kappa^2)/\kappa^2}}{4\pi^2 r} \left(r\cos(\rho r) - \frac{2\alpha^2 \rho}{\kappa^2} \sin(\rho r) \right) \right| \leqslant \frac{e^{2\alpha^2\mu/\kappa}}{4\pi^2} \left(1 + \frac{9\alpha^2}{2} \right). \qquad (75)$$

For the second term in (73) we use (42) and $|f(\rho)| \leqslant \rho e^{2\alpha^2\mu/\kappa}/4\pi^2$ to obtain

$$\left| \int_{\kappa-\mu}^{\kappa+\mu} \sum_{m=1}^{M} w_m (\rho+\kappa) e^{-\tau_m(\rho+\kappa)^2} f(\rho) d\rho \right| \leqslant \frac{e^{2\alpha^2\mu/\kappa}}{4\pi^2} \int_{\kappa-\mu}^{\kappa+\mu} \frac{2\rho}{\rho+\kappa} d\rho \leqslant \frac{\mu e^{2\alpha^2\mu/\kappa}}{\pi^2}. \qquad (76)$$

Combining (74)–(76), and then using $\mu = \min\{\kappa\delta, \delta\}$ and α in (37), and finally, using $b \geqslant \sqrt{3}$, (55) and $c \geqslant 1$, we have

$$|I_3(r)| \leqslant \frac{\mu e^{2\alpha^2\mu/\kappa}}{\pi^2} \left(2 + \frac{9\alpha^2}{2} \right) \leqslant \frac{\delta e^{2\alpha^2\delta}}{\pi^2} \left(2 + \frac{9}{2} \frac{\log\delta^{-1}}{b^2-1} \right) \leqslant \frac{2\delta}{\pi^2} \left(2 + \frac{9}{4}\log\delta^{-1} \right) \leqslant \frac{9\delta}{\pi^2}\log(c\delta^{-1}). \qquad (77)$$

Using Proposition 5, we have

$$I_4(r) \leqslant \left(2 + \frac{1}{r} \right) \delta \log\delta^{-1} \leqslant \left(2 + \frac{1}{r} \right) \delta \log(c\delta^{-1}). \qquad (78)$$

Collecting (71), (72), (77) and (78), we obtain the final result.

In dimension $d = 2$, we estimate the corresponding integrals but using $|J_0(x)| \leqslant 1$. Similar to (71) and (72), we have

$$\left| \frac{1}{2\pi} \int_0^{\kappa-\mu} (\widehat{S}_{\text{oscill}}(\rho) - \widehat{F}_{\text{oscill}}(\rho)) J_0(\rho r) \rho \, d\rho \right| \leqslant \frac{\delta}{4\pi} \log(c\delta^{-1}) \qquad (79)$$

and

$$\left| \frac{1}{2\pi} \int_{\kappa+\mu}^{b\kappa} (\widehat{S}_{\text{oscill}}(\rho) - \widehat{F}_{\text{oscill}}(\rho)) J_0(\rho r) \rho \, d\rho \right| \leqslant \frac{\delta}{4\pi} \log(c\delta^{-1}). \qquad (80)$$

Similar to (74) and (76), we define

$$f(\rho) = \frac{1}{4\pi} e^{-\alpha^2(\rho^2-\kappa^2)/\kappa^2} J_0(\rho r)$$

and use $|J_0(x)| \leqslant 1$, $|J_1(x)| \leqslant 3/(2\sqrt{x})$ (see [31, (4)]), (37), and $b \geqslant \sqrt{3}$ to estimate

$$\max_{x \in [\kappa-\mu,\kappa+\mu]} |f'(x)| \leqslant \frac{e^{2\alpha^2\mu/\kappa}}{4\pi} \left(\frac{3\sqrt{r}}{2\sqrt{\kappa-\mu}} + \frac{2\alpha^2(\kappa+\mu)}{\kappa^2} \right) \leqslant \frac{e^{2\alpha^2\delta}}{4\pi} \left(\frac{2\sqrt{r}}{\sqrt{\kappa}} + \frac{4\log\delta^{-1}}{3\kappa} \right).$$

Thus, using Lemma 20, (63), (55) and $\delta \geqslant \max\{\mu/\kappa, \mu/\sqrt{\kappa}\}$, we obtain

$$\left| \int_{-\mu}^{\mu} \sum_{m=1}^{M} w_m q e^{-\tau_m q^2} f(q+\kappa) dq \right| \leqslant 4\mu \max_{\rho \in [\kappa-\mu,\kappa+\mu]} |f'(\rho)| \leqslant \frac{2\delta}{\pi} \left(2\sqrt{r} + \frac{4\log\delta^{-1}}{3} \right)$$

and, using (64), obtain

$$\left| \int_{\kappa-\mu}^{\kappa+\mu} \sum_{m=1}^{M} w_m (\rho+\kappa) e^{-\tau_m(\rho+\kappa)^2} f(\rho) d\rho \right| \leqslant \frac{e^{2\alpha^2\mu/\kappa}}{4\pi} \int_{\kappa-\mu}^{\kappa+\mu} \frac{2}{\rho+\kappa} d\rho \leqslant \frac{\mu e^{2\alpha^2\delta}}{\pi(2\kappa-\mu)} \leqslant \frac{6\delta}{5\pi}.$$

Thus, we have

$$\left|\frac{1}{2\pi}\int_{\kappa-\mu}^{\kappa+\mu}\widehat{S}_{\text{oscill}}(\rho)J_0(\rho r)\rho\,d\rho\right|\leqslant \delta\log(c\delta^{-1})\left(\frac{58}{15\pi}+\frac{4}{\pi}\sqrt{r}\right). \tag{81}$$

Using Proposition 5 and (79)–(81), we obtain the result. □

A.6. Proof of auxiliary results

Lemma 17. *For $0 < \delta \leqslant 1/2$, any real parameter α, and $r \geqslant 0$ we have*

$$\frac{1}{2\pi^2 r}\left|\text{p.v.}\int_{\kappa-\mu}^{\kappa+\mu}\widehat{F}_{\text{oscill}}(\rho)\sin(\rho r)\rho\,d\rho\right|\leqslant \frac{\delta e^{2\alpha^2\delta}}{2\pi^2}(6+9\alpha^2) \tag{82}$$

in dimension $d = 3$ and

$$\frac{1}{2\pi}\left|\text{p.v.}\int_{\kappa-\mu}^{\kappa+\mu}\widehat{F}_{\text{oscill}}(\rho)J_0(\rho r)\rho\,d\rho\right|\leqslant \frac{\delta e^{2\alpha^2\delta}}{2\pi}\left(\sqrt{6r}+6\alpha^2+\frac{8}{3}\right) \tag{83}$$

in dimension $d = 2$, where $\mu = \min\{\kappa\delta, \delta\}$.

Proof. In order to use Lemma 20, for dimension $d = 3$ we define

$$f(\rho)=\frac{1}{2\pi^2 r}\frac{e^{-\alpha^2(\rho^2-\kappa^2)/\kappa^2}}{\rho+\kappa}\rho\sin(\rho r)$$

and estimate

$$f'(\rho)=\frac{1}{2\pi^2}\frac{e^{-\alpha^2(\rho^2-\kappa^2)/\kappa^2}}{\rho+\kappa}\left(\rho\cos(\rho r)+\frac{\sin(\rho r)}{r}\left(1-\frac{\rho}{\rho+\kappa}-\frac{2\alpha^2\rho^2}{\kappa^2}\right)\right)$$

as

$$\max_{\rho\in[\kappa-\mu,\kappa+\mu]}|f'(\rho)|\leqslant\frac{1}{2\pi^2}e^{2\alpha^2\mu/\kappa}\frac{\kappa+\mu}{2\kappa-\mu}\left(3+2\frac{(\kappa+\mu)^2}{\kappa^2}\alpha^2\right)$$

using $|e^{-\alpha^2(\rho^2-\kappa^2)/\kappa^2}|\leqslant e^{2\alpha^2\mu/\kappa}$ and $|\sin(\rho r)/r|\leqslant\rho$. Since $\mu=\min\{\kappa\delta,\delta\}$ and $\delta\leqslant 1/2$, we have $(\kappa+\mu)/(2\kappa-\mu)\leqslant 1$ and $(\kappa+\mu)^2/\kappa^2\leqslant 9/4$, which yields

$$2\mu\max_{\rho\in[\kappa-\mu,\kappa+\mu]}|f'(\rho)|\leqslant\frac{2\mu}{2\pi^2}e^{2\alpha^2\delta}\left(3+\frac{9}{2}\alpha^2\right)\leqslant\frac{\delta}{2\pi^2}e^{2\alpha^2\delta}(6+9\alpha^2).$$

Similarly, in dimension $d = 2$ we define

$$f(\rho)=\frac{1}{2\pi}\frac{e^{-\alpha^2(\rho^2-\kappa^2)/\kappa^2}}{\rho+\kappa}\rho J_0(\rho r)$$

and estimate

$$f'(\rho)=\frac{1}{2\pi}\frac{e^{-\alpha^2(\rho^2-\kappa^2)/\kappa^2}}{\rho+\kappa}\left(-r\rho J_1(\rho r)+J_0(\rho r)\left(1-\frac{\rho}{\rho+\kappa}-\frac{2\alpha^2\rho^2}{\kappa^2}\right)\right).$$

Using $|J_0(x)|\leqslant 1, |J_1(x)|\leqslant 3/(2\sqrt{x})$ (see [31, (4)]), $1/(\rho+\kappa)\leqslant 2/3\kappa, (\kappa+\mu)^2/\kappa^2\leqslant 9/4$, and then $\sqrt{\kappa+\mu}/\kappa\leqslant\sqrt{3}/\sqrt{2\kappa}$ and $\delta\geqslant\max\{\mu/\kappa,\mu/\sqrt{\kappa}\}$, we obtain

$$2\mu\max_{\rho\in[\kappa-\mu,\kappa+\mu]}|f'(\rho)|\leqslant\frac{2\mu e^{2\alpha^2\delta}}{3\pi\kappa}\left(\frac{3\sqrt{r(\kappa+\mu)}}{2}+2+\frac{9}{2}\alpha^2\right)\leqslant\frac{\delta e^{2\alpha^2\delta}}{2\pi}\left(\sqrt{6r}+\frac{8}{3}+6\alpha^2\right).\quad\square$$

Lemma 18. *For $b > 1$, any real parameter α, and $r \geqslant 0$ we have*

$$\frac{1}{2\pi^2 r}\int_{b\kappa}^{\infty}|\widehat{F}_{\text{oscill}}(\rho)\sin(\rho r)\rho|d\rho\leqslant\frac{e^{-\alpha^2(b^2-1)}}{4\pi^2 r\alpha^2(b^2-1)}$$

in dimension $d = 3$, and

$$\frac{1}{2\pi} \int_{b\kappa}^{\infty} |\widehat{F}_{\text{oscill}}(\rho) J_0(\rho r) \rho| d\rho \leqslant \frac{e^{-\alpha^2(b^2-1)}}{4\pi\alpha^2(b^2-1)}$$

in dimension $d = 2$.

Proof. Using the monotonicity of $1/(\rho^2 - \kappa^2)$ for $\rho \in [b\kappa, \infty)$ in $d = 3$, we have

$$\frac{1}{2\pi^2 r} \int_{b\kappa}^{\infty} |\widehat{F}_{\text{oscill}}(\rho) \sin(\rho r) \rho| d\rho \leqslant \frac{1}{2\pi^2 r} \int_{b\kappa}^{\infty} \frac{\rho e^{-\alpha^2(\rho^2-\kappa^2)/\kappa^2}}{\rho^2 - \kappa^2} d\rho \leqslant \frac{e^{\alpha^2}}{2\pi^2 r \kappa^2 (b^2-1)} \int_{b\kappa}^{\infty} \rho e^{-\alpha^2 \rho^2/\kappa^2} d\rho = \frac{e^{-\alpha^2(b^2-1)}}{4\pi^2 r \alpha^2 (b^2-1)}$$

and, similarly for $d = 2$, we have

$$\left| \frac{1}{2\pi} \int_{b\kappa}^{\infty} \widehat{F}_{\text{oscill}}(\rho) J_0(\rho r) \rho \, d\rho \right| \leqslant \frac{e^{-\alpha^2(b^2-1)}}{4\pi\alpha^2(b^2-1)}. \qquad \square$$

Lemma 19. *For $0 < \tilde{\delta} \leqslant 1$ and $\epsilon_0 > 0$, there exists $\tilde{w}_m > 0$, $\tilde{\tau}_m > 0$ and an integer $\widetilde{N}$ such that*

$$\left| \frac{1}{x^2} - \sum_{m=1}^{\widetilde{N}} \tilde{w}_m e^{-\tilde{\tau}_m x^2} \right| \leqslant \frac{\epsilon_0}{x^2} \tag{84}$$

for $\tilde{\delta} \leqslant x \leqslant 1$,

$$\sum_{m=1}^{\widetilde{N}} \tilde{w}_m e^{-\tilde{\tau}_m x^2} \leqslant \frac{1 + \epsilon_0}{x^2} \tag{85}$$

for $0 \leqslant x < \tilde{\delta}$ and

$$\widetilde{N} \sim \log \epsilon_0^{-1} (\log \epsilon_0^{-1} + \log \tilde{\delta}^{-1}).$$

Proof. See [29]. $\square$

Lemma 20. *For $f \in C^1[-a, a]$, where $a > 0$, we have*

$$\left| \text{p.v.} \int_{-a}^{a} \frac{f(x)}{x} dx \right| \leqslant 2a \max_{x \in [-a,a]} |f'(x)|.$$

Furthermore, for $\tau > 0$ we have

$$\left| \int_{-a}^{a} x e^{-\tau x^2} f(x) dx \right| \leqslant \max_{x \in [-a,a]} |f'(x)| \int_{-a}^{a} x^2 e^{-\tau x^2} dx.$$

Proof. Use the first order Taylor expansion of f about 0. $\square$

References

[1] P. Ewald, Die berechnung optischer und elektrostatischer gitterpotentiale, Ann. Phys. 64 (1921) 253–287.
[2] G. Beylkin, C. Kurcz, L. Monzón, Fast algorithms for Helmholtz Green's functions, Proc. Royal Soc. A 464 (2008) 3301–3326.
[3] G. Beylkin, L. Monzón, On approximation of functions by exponential sums, Appl. Comput. Harmon. Anal. 19 (1) (2005) 17–48.
[4] G. Beylkin, M.J. Mohlenkamp, Numerical operator calculus in higher dimensions, Proc. Natl. Acad. Sci. USA 99 (16) (2002) 10246–10251.
[5] R. Harrison, G. Fann, T. Yanai, G. Beylkin, Multiresolution quantum chemistry in multiwavelet bases, in: P.M.A. Sloot et al. (Eds.), Computational Science-ICCS 2003, Lecture Notes in Computer Science, vol. 2660, Springer, 2003, pp. 103–110.
[6] R. Harrison, G. Fann, T. Yanai, Z. Gan, G. Beylkin, Multiresolution quantum chemistry: basic theory and initial applications, J. Chem. Phys. 121 (23) (2004) 11587–11598.
[7] G. Beylkin, V. Cheruvu, F. Pérez, Fast adaptive algorithms in the non-standard form for multidimensional problems, Appl. Comput. Harmon. Anal. 24 (3) (2008) 354–377.
[8] L. Greengard, J. Strain, The fast Gauss transform, SIAM J. Sci. Statist. Comput. 12 (1) (1991) 79–94.
[9] L. Greengard, X. Sun, A new version of the fast Gauss transform, in: Proceedings of the International Congress of Mathematicians, vol. III (Extra Vol.), 1998, pp. 575–584.
[10] J. Strain, The fast Gauss transform with variable scales, SIAM J. Sci. Statist. Comput. 12 (5) (1991) 1131–1139.
[11] G. Beylkin, C. Kurcz, L. Monzón, Grids and transforms for band-limited functions in a disk, Inverse Probl. 23 (5) (2007) 2059–2088.
[12] G. Beylkin, On the fast Fourier transform of functions with singularities, Appl. Comput. Harmon. Anal. 2 (4) (1995) 363–381.
[13] A. Dutt, V. Rokhlin, Fast Fourier transforms for nonequispaced data, SIAM J. Sci. Comput. 14 (6) (1993) 1368–1393.
[14] J.-Y. Lee, L. Greengard, The type 3 nonuniform FFT and its applications, J. Comput. Phys. 206 (1) (2005) 1–5.
[15] V. Rokhlin, Diagonal forms of translation operators for the Helmholtz equation in three dimensions, Appl. Comput. Harmon. Anal. 1 (1) (1993) 82–93.
[16] L. Greengard, J. Huang, V. Rokhlin, S. Wandzura, Accelerating fast multipole methods for the Helmholtz equation at low frequencies, IEEE Comput. Sci. Eng. 5 (3) (1998) 32–38.

[17] H. Cheng, W.Y. Crutchfield, Z. Gimbutas, L.F. Greengard, J.F. Ethridge, J. Huang, V. Rokhlin, N. Yarvin, J. Zhao, A wideband fast multipole method for the Helmholtz equation in three dimensions, J. Comput. Phys. 216 (1) (2006) 300–325.
[18] M. Cátedra, R. Torres, J. Basterrechea, E. Gago, The CG-FFT Method, Artech House, 1995.
[19] O.P. Bruno, H.E. McKay, Higher-order Fourier approximation in scattering by two-dimensional, inhomogeneous media, SIAM J. Numer. Anal. 42 (6) (2005) 2298–2319.
[20] F. Andersson, A. Holst, A fast, bandlimited solver for scattering problems in inhomogeneous media, J. Fourier Anal. Appl. 11 (4) (2005) 471–487.
[21] F. Lanzara, V. Maz'ya, G. Schmidt, Numerical solution of the Lippmann–Schwinger equation by approximate approximations, J. Fourier Anal. Appl. 10 (6) (2004) 645–660.
[22] Y. Chen, A fast, direct algorithm for the Lippmann–Schwinger integral equation in two dimensions, Adv. Comput. Math. 16 (2–3) (2002) 175–190.
[23] I.M. Gel'fand, G.E. Shilov, Generalized Functions, vol. 1, Academic Press, New York, 1964. Properties and Operations, Translated from the Russian by Eugene Saletan.
[24] L. Grafakos, Classical and Modern Fourier Analysis, Pearson Education, Inc., 2004.
[25] G. Beylkin, L. Monzón, On generalized Gaussian quadratures for exponentials and their applications, Appl. Comput. Harmon. Anal. 12 (3) (2002) 332–373.
[26] T. Darden, D. York, L. Pedersen, Particle mesh Ewald: an $n \log(n)$ method for Ewald sums in large systems, J. Chem. Phys. 98 (12) (1993) 10089–10092.
[27] M. Silveirinha, C. Fernandes, A new acceleration technique with exponential convergence rate to evaluate periodic Green functions, IEEE Trans. Antennas Propag. 53 (1) (2005) 347–355.
[28] M. Abramowitz, I.A. Stegun, Handbook of Mathematical Functions, ninth ed., Dover Publications, 1970.
[29] G. Beylkin, L. Monzón, Approximation of functions by exponential sums revisited, in preparation.
[30] I. Gradshteyn, I.M. Ryzhik, Table of Integrals, Series, and Products, fifth ed., Academic Press, 1994.
[31] A.Y. Olenko, Upper bound on $\sqrt{x}J_{\nu}(x)$ and its applications, Integr. Transforms Spec. Funct. 17 (6) (2006) 455–467.